2024-09-02

Structural and geomorphological constraints on the activity of the Sparta Fault (Greece)

Çal Çağatay

Sarah Boulton *School of Geography, Earth and Environmental Sciences*

Zoe Mildon *School of Geography, Earth and Environmental Sciences*

Structural and geomorphological constraints on the activity of the Sparta Fault (Greece)

Çağatay, Çal; Boulton, Sarah; Mildon, Zoe

Published in:
Journal of the Geological Society

DOI:
10.1144/jgs2024-066

Publication date:
2024

Document version:
Peer reviewed version

Structural and geomorphological constraints on the activity of the Sparta Fault (Greece)

Çağatay Çal[1,2], Sarah J. Boulton[1],*, Zoë Mildon[1]

[1]School of Geography, Earth and Environmental Sciences, University of Plymouth, Drakes Circus, Plymouth, PL4 8AA.

[2] Now at the Department of Geological Research, General Directorate of Mineral Research and Exploration (MTA), Ankara, TR, 06800, Türkiye

*Correspondence: sarah.boulton@plymouth.ac.uk

The ancient city of Sparti (Greece) suffered extensive damage from a M_w ~7.2 earthquake in 464 B.C.E. resulting in ~ 20,000 fatalities, but questions remain on the short (~10^4 yrs) and long-term (10^5 – 10^6 yrs) activity of this important structure. This paper presents new structural data and fluvial geomorphologic analysis from the Sparta Fault, and in particular considers the northern fault segment that is less well known. A new topographic profile on the well-developed post-glacial fault scarp from the northern strand indicates a 7.53 m offset over the last ~15 ka, suggesting a throw rate of ~0.5 mm/yr. The longitudinal profiles of rivers flowing across the fault allow elucidation of longer-term fault activity. Along the strike of the fault rivers exhibit up to two slope-break knickpoints, which decrease in height from south to north. These knickpoints are interpreted to have formed owing to the initiation of faulting and a subsequent slip-rate acceleration. The post-glacial fault scarp and fluvial geomorphology both indicate that entire fault is active and has an asymmetrical throw profile that results in the highest slip-rate in the south.

Keywords: Active faulting; Normal fault; River profiles; Fluvial geomorphology; Greece.

Supplementary material: [Structural measurements along the Sparta Fault] is available at...

In 464 B.C.E, the ancient city of Sparti (Greece) suffered extensive damage from an estimated M_w ~7.2 earthquake resulting in ~ 20,000 fatalities (Armijo *et al*., 1991) and potentially precipitating the first Peloponnesian war (Armijo *et al*., 1991). Although no further earthquakes have significantly ruptured the causative Sparta Fault since the 464 B.C. event (Papanastassiou, 1998), the recurrence interval of major earthquakes along the fault is calculated to be > 2500 years (Benedetti *et al*., 2002) based on ^{36}Cl studies, or 1792 ± 458 years (Papanikolaou *et al.*, 2013) based on throw rates. This long recurrence interval and the time since the last event may suggest that the fault could rupture again in the next few hundreds of years, posing significant hazard to the modern city of Sparta and the surrounding region. Yet, despite the compelling historical record and clear geohazard posed by this structure, few studies have been undertaken on the Sparta Fault and these have mainly focused on the southern section of the fault (e.g., Armijo *et al*., 1991; 1992; Papanastassiou, 1998; Benedetti *et al*., 2002; Papanastassiou *et al*., 2005; Papanikolaou *et al*., 2013). These studies have mainly investigated either the exposed fault scarp that is related to fault activity since the Last Glacial Maximum (LGM, ~15 ± 3 kyr) using ^{36}Cl cosmogenic nuclide analysis to evaluate slip over the Holocene (Benedetti *et al.*, 2002), or the tectonic geomorphology of the region using Digital Elevation Models [DEMs] (e.g., Papanikolaou *et al*., 2013).

This paper extends the existing knowledge on the Sparta Fault by using a combination structural geology, tectonic and fluvial geomorphology to investigate the longer (~ 10^5 -10^6 years), and shorter (~ 10^4 years) term activity and evolution of this seismogenic structure along the entire length of the fault, including the less-well studied northern section. New structural data are presented defining the morphology and kinematics of the fault scarp. A new post-glacial scarp profile of the Sparta Fault is presented along with previous data to inform the short-term (Holocene, ~10^5 years) fault activity. Finally, the fluvial morphology of rivers flowing across the Sparta Fault are investigated and evaluated to give information on the on the medium to long term (~10^6 years) fault activity. These data demonstrate that the northern segment of the Sparta Fault is more active than previously recognised over short and long timescales. In addition, the geometry of the fault is variable along strike. These observations have significant implications for the determination of regional seismic hazard.

Geological Background

The Hellenic Arc is the active plate boundary between the Eurasian plate in the north and the African plate in the south (Reilinger *et al.*, 1997; Papanikolaou *et al*., 2004). Current rates of plate convergence are in the order of ~20-30 mm/year (Reilinger *et al.*, 1997, 2006; McClusky *et al.*, 2000; Agostini *et al*., 2010; Gürer *et al*., 2022) with the subduction of the remnant oceanic crust of the Eastern Mediterrenean below the Hellenic Arc. Trench rollback along the arc results in regional upper plate extension (Jolivet and Brun, 2010), which in the Peloponnese region has resulted ~ E-W extension (Papanikolaou and Royden, 2007) and a series of normal faults defining a series of NW-SE trending neotectonic horsts and grabens (Lyon-Caen *et al.*, 1988; Papanikolaou *et al.*, 1988).

The Sparta Fault is a normal fault with an overall NNW - SSE trend forming the eastern margin of the Taygetos neotectonic horst and the western margin of the Sparta (or Evrotas) Basin (Fig. 1) (Lyon-Caen, 1988; Papanikolaou *et al.*, 1988). In map view, the fault has a sinuous shape composed of left-stepping en-echelon segments striking at ~350° coupled to shorter segments striking at ~320° (Armijo *et al*., 1991). The Eurotas River flows parallel to the Sparta Fault and its tributaries cross the fault (Fig. 1). In addition, there is a minor antithetic fault system that is located on the eastern margin of the graben ~5 km to the east of the Sparta Fault (Papanikolaou *et al*., 2013).

The Sparta Fault mainly follows the outcrop extent of the Miocene units of the Taygetos Mountain (Papanikolaou and Royden, 2007). The fault is divided into various segments based on the segment's strike and/or the Alpine units exposed in the hanging wall and/or footwall (Papanikolaou and Royden, 2007; Papanikolaou *et al*., 2013). The units exposed in the Taygetos Mountains include the Mani autochthon (Fig. 3) and the Arna, Tripolis and Pindos nappes (Papanikolaou and Royden, 2007).

These basement units mainly consist of Jurassic-Cenomanian-aged flysch, Upper Cretaceous to Upper Maastrichtian limestones, and Eocene-Oligocene flysch (Deligiannakis, 2011). The Arna Unit is composed of phyllites, schists, and metabasalts of Permian-Lower Jurassic age (Papanikolaou and Skarpelis, 1987) and is considered to be the metamorphic basement of the Tripolis unit (e.g., Tataris *et al*., 1970; Psonis, 1986; Psonis, 1990). The unit outcrops in limited areas along the footwall of the fault and is overlain by the Tripolis nappe unit throughout the study area.

The base of the Tripolis Nappe is marked by a Permo-Triassic volcano-sedimentary rift-associated unit, the Tyros bed, overlain by dolomitic limestones, dolomites and limestones, which are dated to the Middle – Upper Triassic and Lower – Middle Eocene (Psonis, 1990; Koutsovitis *et al*., 2020). The top of the Tripolis Nappe is composed of Upper Eocene – Oligocene-aged flysch. Similarly, the Mani Unit is autochthonous and consists of marbles, phyllitic crystalline basement, limestones and turbidites representing the metamorphic equivalent of the Ionian zone (Papanikolaou, 1986). The Pindos Nappe is similarly composed of turbidites and limestones, which in the Peloponnese date to the Palaeocene (Piper, 2006).

In the southern section between the villages of Anogia and Mystras, and from Vordonia to Kastori (Figs 1-2), the Sparta Fault separates the Mani Unit in the footwall from Plio-Quaternary deposits covering the metamorphics of Arna Units in the hanging wall. In contrast, in the central section of the fault from Mystras and Vordonia (Fig. 2), the footwall is variably composed of the Arna Nappe or the Mani Unit and the hanging wall comprises overlying Plio-Quaternary sediments with some outcrops of the Arna Unit, representing a lower throw than to the south (Papanikolaou *et al.*, 2013). The footwall from Logkanikos (Fig. 2) to the northern tip of the fault consists of Tripolis Mesozoic-aged limestone, while the hanging wall of the fault in this area is composed of Tripolis Eocene-aged flysch and in some locations overlying the Pindos nappe (Papanikolaou *et al.*, 2013).

In general, the stratigraphic units demonstrate that the present-day high-angle Sparta Fault accommodates ~2 km throw (Papanikolaou *et al.*, 2013) that has accumulated probably since the Early Pliocene based upon the basin fill (Piper *et al.*, 1982), though the exact timing of the fault initiation is unclear.

Geomorphologic Background

The Quaternary activity of the Peloponnese region has been described by many researchers (e.g., Armijo *et al.,* 1991; Maroukian *et al.*, 1999; Pope *et al.*, 2003; Hughes *et al.*, 2005; Pope and Wilkinson, 2005) with a number of morphotectonic and geologic studies conducted along the Sparta Fault, including alluvial fan geomorphology and Quaternary sedimentation (Piper *et al.*, 1982; Pe-Piper and Piper, 1985; Pope and Millington, 2000; 2002; Pope, 2003), fluvial geomorphology (Papanikolaou *et al.*, 2013), post-glacial slip history using ^{36}Cl cosmogenic dating (Benedetti *et al.*, 2002), and palaeoseismological trenching (Papanastassiou *et al.*, 2005).

Strikingly, the Taygetos Mountain front illustrates clear triangular and trapezoidal facets, V-shaped and 'wine-glass canyons' that are indicators of high uplift rates (i.e., Armijo *et al.,* 1991). The triangular facets consist of three sets with slopes of 20°, 30° and 40° at 725, 450 and 250 m elevation, respectively (Armijo *et al.*, 1991), likely representing the decreasing age of the facets (Papanastassiou *et al.*, 2005). Additionally, steep alluvial talus cones issuing from the canyons and scree slopes are described along the range front (Papanastassiou *et al.*, 2005). Papanastassiou *et al.* (2005) identified two generations of alluvial fans, where the slope of the older fans is 3° and the slope of the younger fans is between 3°- 6°. The oldest fans consist of repetitive upwards breccia, the deposition of which is suggested to couple with prior earthquakes.

Additionally, the Sparta Fault has a significant post-glacial bedrock fault scarp preserved along much of the strike of the fault (e.g., Armijo *et al*., 1992; Benedetti *et al*., 2002; Papanikolaou *et al*., 2013). Similar post-glacial fault scarps have been described throughout the eastern Mediterranean area, the result of differential erosion between glacial and interglacial periods (Roberts and Michetti, 2004). During glacial conditions, rates of erosion and sedimentation were high and greater than fault throw-rates. As a result, escarpments formed by coseismic slip were degraded or covered rapidly (Roberts and Michetti, 2004). Vegetation was also extremely rare because of the cold climate conditions further increasing soil instability. It should be noted that though glacial features have been described in the Taygetos Mountains, the snow line was likely no lower than 2000 m (Mastronuzzi *et al.*, 1994). After the end of the LGM (~15 ± 3 kyr), rates of erosion and sedimentation declined relative to fault throw-rates, thus fault surfaces were progressively exhumed and preserved. The ages of individual fault scarps can be estimated from ^{36}Cl cosmogenic analyses, and across the Mediterranean the scarp ages are broadly consistent (e.g., Schlagenhauf *et al*., 2011; Cowie *et al*., 2017; Mechernich *et al*., 2023), although recent research indicates that fault scarps generally decrease in age with increasing elevation (Iezzi *et al*., 2019). Results derived from the Sparta Fault and the Pisia Fault (Perachora peninsula, Greece) indicate that these scarps are 13 kyr and 21-29 kyr old respectively (Benedetti *et al*., 2002; Mechernich *et al*., 2018).

The post-glacial scarp of the Sparta Fault is reported to have a steepness of 65°- 68° and a maximum height of 10-12 m (Benedetti *et al*., 2002). However, Papanikolaou *et al*. (2013) described a lower activity section in the northern part of the fault owing to a lack of a post-glacial fault scarp. The southern and central sections of the fault have been described by Papanikolaou *et al.* (2013) as having a considerable post-glacial escarpment height from 8 to 12 m and a variable dip (38°- 80°). In addition, they interpret the central and southern segments as being hard-linked.

The slip history of the Sparta Fault was evaluated by Benedetti *et al*. (2002) using the fault scarp exposed in southern sections of the fault. ^{36}Cl cosmogenic nuclide analyses were applied to samples taken from locations close to Anogia and Parori (Fig. 2). Benedetti *et al*. (2002) determined that four earthquakes have taken place at the Parori site at 2.8 ± 0.3 kyr, 4 kyr, 4.5 kyr, 5.9 kyr, and four earthquakes occurred at Anogia at 4.5 kyr, 5.9 kyr, 8.4 kyr, 12.9 kyr. At both locations the 4.5 kyr and 5.9 kyr events were present. The 2.8 kyr event, only recognised at Parori, is interpreted by Benedetti *et al*. (2002) to be the slip from the last earthquake in 464 B.C.E. Although the effects of this earthquake are not seen in the ^{36}Cl data from Anogia, Benedetti *et al*. (2002) note that there is evidence of minor hangingwall scarps 10-20 m below the primary bedrock scarp, which may indicate that the 464 B.C.E. event bypassed the main scarp at this location.

These data allow the slip-rate on the Sparta Fault over the last ~13 - 15 ka to be determined, the rate of the southern section of the Sparta fault is between 0.5 mm/yr and 2 mm/yr (Benedetti *et al.*, 2002). Using scarp profiles across the post-glacial scarp, Papanikolaou *et al*. (2013) determined the throw rate in the southern section (close to the village of Anogia) to be 0.55 – 0.65 mm/yr. For the northern section of the Sparta fault, these authors hypothesise that the slip rate is < 0.3 mm/yr.

Significantly, the Sparta region has experienced low seismicity since the 464 BCE earthquake. In fact across the wider Peloponnese, only thirty-one earthquakes have been recorded with M_w > 5.0 over the instrumental period, from 1925 – 2023 (https://earthquake.usgs.gov/earthquakes). The highest magnitude instrumental earthquake recorded in the region was M_w = 7.3 with a depth of 15 km in 1947 near Koroni, which is ~50 km west of Sparta. Another substantial earthquake happened in 1986, a M_s = 5.9 in Kalamata city, west of Taygetos Mt. (Lyon-Caen, 1988).

Fluvial Geomorphology

Tectonic geomorphology seeks to understand how landscapes respond to changing boundary conditions, such as climate change, tectonics, or sedimentary processes. In particular, the relationship between landscapes and river systems, which play a significant role in landscape evolution, can be a sensitive recorder of long-term landscape change (Tucker and Whipple, 2002). As a result, a number of erosion 'laws' have been defined since the early 1980s (Howard and Kerby, 1983; Whipple and Tucker, 1999a; Whittaker *et al.*, 2007). Despite diversity in the number and detail of such erosion laws or models, most aim to characterize the long term pace of channel erosion, which is a function of catchment size and channel gradient (Howard and Kerby, 1983).

The study of river systems is crucial for understanding the tectonic response of the landscape. Rivers are grouped into three categories in terms of their channel morphology: alluvial (transport-limited) channel; bedrock (detachment-limited) channel, and mixed channel (Howard *et al.*, 1994). This research is focused on bedrock channels because of the well-characterized response of such rivers to active tectonics (Kirby and Whipple, 2001, 2012; Whipple, 2001, 2004; Whittaker *et al.*, 2007).

Detachment-limited channels have been studied using a stream power model that relates the vertical incision rate of the bedrock (ε) to catchment area (A), river gradient (S) (Howard and Kerby, 1983), where:

$$\varepsilon = KA^mS^n \qquad \text{(eq. 1)}$$

m and n are positive values that are associated with watershed hydrology, hydraulic geometry, and abrasion (Kirby and Whipple, 2001), and the coefficient of erosion (K) is related numerous factors including lithology, climatic factors, river channel structure and sediment supply (Whipple and Tucker, 2002; Whipple, 2004).

River channels can be described as being either steady state or having transient conditions (Whipple and Tucker, 1999). Steady-state conditions, proposed by Hack (1957) as dynamic equilibrium in which uplift of the region is balanced by erosion, are characterized by concave-shaped river longitudinal profiles in which channel elevation decreases progressively from source to base level, such as a river, sea or lake.

Longitudinal profiles of detachment rivers can be formulised by using the stream power model (eq. 1), which relates channel gradient, S, and catchment area, A, by equation 2 (Flint, 1974):

$$S=k_sA^{-\Theta} \qquad \text{(Eq. 2)}$$

k_s is the steepness index which has been linked with deposit supply, rainfall, rock durability, uplift throughout the channel and Θ is concavity index. Typically concavity varies in the range of 0.1 to > 1, with detachment-limited channels typically demonstrating θ values from 0.3 to 0.7 (Bierman and Montgomery, 2020).

If a river is in steady-state, a single concavity value will represent the whole river. However, individual rivers in an area may have different concavities (Wobus, Crosby and Whipple, 2006), requiring the use of a specific concavity index value (typically 0.45) in order to calculate normalized steepness indices (k_{sn}) of the channel allowing the comparison between rivers across a given study area.

Conversely, transient landscapes form when uplift and erosion are unbalanced in a bedrock channel because of changing boundary conditions, such as tectonic uplift, climatic gradients, lithological variation or landslides effecting erosion rates in the channel. As a result of variable rates of erosion along the channel, a knickpoint forms separating the erosional domains (Whipple and Tucker, 1999a). Two forms of knickpoint can be defined: vertical-step knickpoints and slope-break knickpoints.

Vertical-step knickpoints are described by an abrupt elevation change of a metre to hundreds of metres (Whipple *et al.,* 2013). Such knickpoints develop because of variable streamflow speed, aggradation and degradation processes mainly as a result of bedrock strength contrasts in the riverbed (Haviv *et al.*, 2010). Vertical-step knickpoints can also correlate with the location of faults, where there is a strong lithological contrast along the structure, landslides or tributaries (Kirby and Whipple, 2012; Liu *et al.*, 2020). They are broadly consistent with smaller channels, commonly step-pools and cascades (Whipple *et al.,* 2013) than regional scale base-level change (Kirby and Whipple, 2012). When observed on log slope – log area graphs, these knickpoints can be quickly identified as a localised increase in steepness causing a spike in slope values (Whipple, 2004). However, critically these knickpoints are generally stationary, fixed on the causative perturbation and do not independently migrate through the river system (Kirby and Whipple, 2012).

By contrast, slope-break knickpoints display a discernible step in the regression lines on a slope-area graph and are caused by an elevation change that forces the river system towards new equilibrium conditions (Tucker and Whipple, 2002; Kirby and Whipple, 2012). Changing boundary conditions can be the effect of uplift as a consequence of new faults, or increasing slip-rate on pre-exisiting faults, or falling base-level (Wobus, Hodges and Whipple, 2003; Marliyani, Arrowsmith and Whipple, 2016).

Slope-break knickpoints transmit the new base level to the catchment as an erosional wave throughout the system. The horizontal celerity is a function of catchment area, thus the knickpoint migration rate along the river system decreases as drainage area declines (Whipple and Tucker, 1999b; Crosby and Whipple, 2006). By contrast, the vertical rate of knickpoint migration can be correlated with fault slip rate (Whittaker and Boulton, 2012) as such the vertical distributions of knickpoints are a consequence of uplift rate distribution along the causative faults. However discrepancies in distribution of knickpoints horizontally and vertically are common due to regional uplift, climatic effects along a region or antecedent topography that was not in steady-state (Bishop *et al.*, 2005). Prevous research by Papanikolaou *et al*. (2013) indentified that some rivers crossing the Sparta Fault contain knickpoints but did not indentify their form. Herein we aim to identify the type of knickpoint and use this to infer long-term fault behaviour.

Methodology

Fluvial geomorphology

A 30m Japanese Aerospace Exploration Agency (Jaxa) ALOS World 3D30 satellite (UTM zone 34 N) DEM was obtained from https://www.eorc.jaxa.jp/ALOS/en/aw3d30/data/index.htm and used for fluvial analysis as Boulton and Stokes (2018) demonstrated that the ALOS World 3D30 DEM is a more accurate for fluvial analyses compared to TanDEM-X or SRTM DEMs for mountainous areas. A Matlab Topotoolbox module (available from https://topotoolbox.wordpress.com/download) and ArcGIS Pro software were used to extract fluvial networks. Topotoolbox implements a group of Matlab commands that are used for analysing geological features in DEMs (Schwanghart, 2014; Schwanghart and Scherler, 2014). k_{sn}*profiler* codes part of the Topographic Analysis Kit (TAK), which leverages the power of Topotoolbox, are utilised for the determination of channel steepness index and location of knickpoints for each river (Forte and Whipple, 2019) through the analysis of slope-area plots. The concavity index is fixed at 0.45 as per other studies (Wobus *et al.*, 2003; DiBiase *et al.*, 2010; Papanikolaou *et al.*, 2013) and a threshold drainage area was set at 10^5 m^2. Although this area is < 10^6 m^2, the value is consistent with the threshold drainage area where the transition from debris-flow dominated to fluvial dominated processes take place in the study area, as determined from analysis of slope-area plots. The same threshold drainage area has also been effectively applied by other similar regional studies (i.e., Gallen and Wegman, 2017; Basmenji *et al.*, 2021).

Fieldwork

Fieldwork generally focused on measuring the post-glacial bedrock scarp of the Sparta Fault. Locations were recorded via Garmin handheld GPS, which has an accuracy of ± 3m. Fault orientation (dip/dip direction), and trend/plunge of striations were measured via Silva compass, angle of declination was adjusted +4° for the study area, and the accuracy of the compass is ±2°. Where possible multiple measurements were taken on each plane to determine a robust mean, calculated using Stereonet v. 11.5.4 (Allmendinger et al., 2013; Cardozo and Allmendinger, 2013). A topographic profile was constructed at a geomorphically-suitable site using a 1 m-long ruler and chain-surveying techniques. This profile is used to calculate the amount of post-glacial throw, and therefore determine the throw rate. Error on throw measurement derived using this technique is ~ 20% (Roberts and Michetti, 2004).

At many locations across the fault, it is not possible to measure a topographic profile because of dense vegetation and/ or steep morphology. At these sites a Trupulse200L laser range finder, which measures slope distance (SD), slope inclination (INC), horizontal distance (HD) and vertical distance (VD) can be used to estimate scarp height in the field. It should be noted that these measurements are a *minimum* estimate of throw as the full profile has not been characterized and therefore cannot be used to calculate throw rates.

Results

The Sparta Fault was investigated at 23 locations (Fig. 3), resulting in a database comprising 198 measurements for the orientation of the exposed fault plane and 77 measures of the slip vector from either slickenlines or determined from small scale (<1m) corrugations on the fault surface (Supplemental Data).

On average the strike of the fault varies between 257° and 009°, with an along strike average of 317°, with an average dip direction of 043° (Table 1; Fig. 4a). Interestingly, the angle of dip varies between 31 - 71° (Fig. 4b), with the highest values occurring near the villages of Anogia and Parori along the southern fault segment and close to Longkanikos on the northern segment. Lows in the angle of dip occur between these in the centre of the fault and towards the fault tips and correspond to similar broad variations in the strike direction. It was not possible to determine the slip direction of the fault at all locations. In general, the slip vector is towards the north-east/east-north-east with trends between 32 – 61° (Fig. 3).

Fault scarp morphology

This section describes in more detail the post-glacial morphology of the Sparta Fault, representing the most recent deformation along the structure. All the observations are given in order from south to north along the fault.

The Anogia section is located near the southern tip of the Sparta Fault and is the first location where a clear post-glacial scarp can be identified. Towards the southern fault tip (Fig. 5A), exposures of the fault plane are present in road cuttings and other excavated banks but no naturally-exhumed scarp was identifiable. At Anogia the scarp can be traced for > 1 km and forms a largely unweathered free face with poorly developed slickenlines. The ^{36}Cl sampling site of Benedetti *et al.* (2002) can be easily located behind the village, where they collected samples up the scarp over 6 m. The scarp throw was measured by Papanikolaou *et al*. (2013) at two locations in the vicinity a few 10's of metres apart as having a post-glacial throw of 8.2 ± 1.6 and 9.7 ± 1.9 m.

As the scarp is traced northwards, it is variably visible as a free face or an oversteepening in the topography. Yet the presence of alluvial fans and channels, anthropogenic modification of slopes, or steep topography prevents the accurate measurement of the post-glacial fault scarp (Fig. 5B). This is the case north of Kalvia Sochas, 4.5 km north of Anogia (34S 0627132 4095666). The fault scarp is clear and can be traced at the base of the range front along the back of olive groves. It is not overly weathered and has clear slickenlines; however, the steep topography prevents construction of a topographic profile. The Trupulse laser range finder estimates of the vertical height of the scarp range from 7 – 11 ± 0.02 m, giving a minimum throw along this section.

From this section to the village of Parori the post-glacial fault scarp is largely absent. It reappears south of Parori along a very steep and highly vegetated hillside (Fig. 5C). The Trupulse again was used to estimated the vertical height of the scarp as 9.6 ± 0.02 m.

Benedetti et al., (2002) also undertook ^{36}Cl sampling near this village, and reported a scarp height 10.7 m (measured in the plane of the fault).

North of Parori, naturally exposed sections of the fault scarp are scarce and the topographic expression of the fault is indistinct. However, the fault scarp is easily located along a number of road cuttings and embankments allowing measurement of the orientation and slip vector of the fault (e.g., Fig. 5D). Near Moni Ampleki, a degraded but geomorphically-clear post-glacial fault scarp was identified in a forest on the northern section of the Sparta Fault (Fig. 5E). The scarp is developed in limestone of the Tripolis Unit, which is well exposed in the footwall but not in the hangingwall (though the lithology is expected to be the same across the fault in this location). The scarp can initially be clearly seen in a road section (Fig.5F) where slickenlines indicate an average plunge and trend of 61°/009° with the plane orientated at 258°/64°N. The fault scarp can be traced eastwards along a natural exposure into the adjacent woodland for > 30 m. At 0608359 4125467 UTM Zone 34N, an eroded but identifiable free face was located that was suitable for constructing a topographic profile, i.e., planar lower and upper slopes, horizontal contact between the fault scarp and lower slope, limited or no evidence of erosive or depositional features such as gullies or landslides (e.g., Bubeck et al., 2015). Here the fault strikes 272° with a dip angle of 62-65°. A topographic profile was constructed parallel to the slip vector (~ 061°, determined from small-scale (<1m) corrugations) across the scarp as the upper and lower slopes are exposed and undisturbed. The interpreted topographic profile gives the throw as 7.53 ± 1.51 m at this location in the northern segment of the Sparta Fault (Fig. 6).

River profile analysis

To investigate the longer-term evolution of the Sparta Fault, 18 rivers tributaries of the Eurotas River were extracted from the ALOS World 3D30 DEM that cross the active fault (Fig. 7A) ranging in length from 15.5 – 2.8 km with corresponding drainage areas from 36.5 – 1.9 km^2. The rivers flow perpendicularly ~west to east across the Sparta Fault into the Sparta Basin, where they join the trunk river system flowing from north to south. The length of the rivers generally increases from the north to the south, though the longest river (river 10) is located in the centre of the fault.

All the rivers extracted contain at least one significant knickpoint, and many rivers contain two or more large-scale knickpoints (Table 2; Figs 7 – 9). In cases where two or more knickpoints observed in the river profiles, the lowest elevation knickpoint is commonly observed at, or close to the mapped location of the Sparta Fault (Fig. 7, 9C) and there is a decrease or no change in k_{sn} downstream of the knickpoint. Additionally, when viewed on a SA plot there is a spike in the slope values at the location of this lowest knickpoint. This knickpoint morphology is characteristic of vertical-step knickpoints.

By contrast, where knickpoints are observed at higher elevations the average normalised steepness index (k_{sn}) = 146.9 $m^{0.9}$ downstream of the knickpoints; while upstream of the knickpoint the average k_{sn} = 87.5 $m^{0.9}$. This increase in k_{sn} downstream of the knickpoint is a characteristic feature of a slope-break knickpoint and is consistent with observations of steep gorges and narrow channels upstream of the fault/downstream of the knickpoint (Fig. 9A), and less incised rivers upstream of the knickpoint (Fig. 9B). It is also important to note that the position of these knickpoints does not correlate with the mapped location of lithological boundaries.

Along seven rivers, two slope-break knickpoints can be observed, these rivers are predominantly found in the central and northern sections of the fault. Using these knickpoints as a guide, the knickpoints along the rivers can be divided into two discrete populations. The first a higher knickpoint generation generally at >1000 m in elevation, and the second lower knickpoint generation at <1000 m in elevation (Fig. 10A); where the average k_{sn} upstream of the higher knickpoint is 88.9 $m^{0.9}$ and below k_{sn} = 148.5 $m^{0.9}$, while for the lower knickpoint the average k_{sn} upstream = 110.6 $m^{0.9}$ and below k_{sn} = 184.5 $m^{0.9}$, showing a progressive steepening of the rivers downstream.

Although, the elevation above sea level of these knickpoints is broadly constant along strike, it is important to note that the elevation of the fault increases towards the north, from ~270 m at river 1 to ~700 m at rivers 17/18. As a result, the height of the knickpoint (the elevation difference between the fault and the knickpoint) decreases along strike from south to north (Fig. 10B) for both the higher and lower elevation knickpoints. Linear regression lines through these data also demonstrate that difference in height between the two knickpoints is consistently ~ 400 m along the strike of the Sparta fault (Fig. 10B). Similarly, weak ($r^2 < 0.2$) along-strike patterns in k_{sn} can be observed (Fig. 10C). Interestingly, the normalised steepness index upstream of the higher knickpoint decreases to the north (from > 150 to < 20 $m^{0.9}$), yet k_{sn} downstream of the lower knickpoint is broadly constant. Additionally, the steepness index characterising the rivers essentially between the two sets of knickpoints is also consistent along the strike of the range. The k_{sn} ratio across the upper knickpoints (Fig. 10D) also shows a slight increase from south to north. Whereas the k_{sn} ratio for the lower knickpoints is constant along the strike of the fault. Interestingly, the average k_{sn} ratio for the lower knickpoints is 2.5, while for the lower it is 1.8.

When analysing mobile knickpoint formation and behaviour, the horizontal and vertical components of knickpoint retreat rate also need to be examined. When the upstream distance of each knickpoint from the fault is plotted against total drainage area of the river catchment (Fig. 11A), it is apparent that the knickpoints have migrated further when drainage area is higher and that the two populations of knickpoints plot with different regressions (significant at 95%; $r^2 \geq 0.5$). This behaviour is consistent with many other studies (e.g., Crosby and Whipple, 2003; Whittaker and Boulton, 2012; Kent *et al*., 2017; Boulton *et al*., 2020) and with theoretical predictions for river behaviours where $L = A^{0.5}$. As the upper and lower knickpoints can be fitted by two different regression lines this suggests that the knickpoints were generated by two distinct events along the fault. Similar scaling relationships are observed when the downstream distance from the drainage divide is plotted against the catchment area upstream of the knickpoint (Fig. 11B), though the correlation is stronger for the lower knickpoints compared to the higher.

When the relationship between the height of the knickpoints and the catchment areas of their rivers is examined (Fig. 11C), to investigate the vertical component of knickpoint migration, there is a weak positive correlation (r^2=0.1) for the lower knickpoints but a strong positive correlation (r^2=0.7) for the higher knickpoints. This shows that knickpoint heights are decreasing with total catchment area. Similarly, when knickpoint height is compared to the upstream distance of the knickpoint from the fault (Fig. 11D), the lower knickpoints are closer to the fault. Interestingly in this case the knickpoints for the higher and lower knickpoints have very similar trends, although the trend line for the upper knickpoints is skewed by an outlier.

Discussion

Implications for seismic hazard

To investigate how fault geometry and slip rates can affect the earthquake rates (an important ingredient in seismic hazard assessment), the Matlab-based FiSH code (Pace et al., 2016) was used to calculate the annual rates of earthquake occurrence. In particular, we focus on the question of how the variations in dip measured along the Sparta fault (Fig. 4) may affect the resultant seismic hazard.

The FiSH code assumes that the seismogenic potential of the fault is based on its geometric and kinematic features, i.e., its dimensions (length, depth), geometry (dip) and slip rate, all of which can be measured from field studies. Measurements show that the dip of the Sparta fault is highly variable, from 31° to 67°, with broadly lower dips in the central region, just north of Sparta (Fig. 4). However, it is not known how this variable dip manifests at seismogenic depths. To explore how the seismic hazard may be affected by the dip, two models are produced using the FiSH code with the minimum and maximum dip values measured in the field. Throw profiles from Papanikolaou *et al*. (2013) and this study are used to derive minimum and maximum slip rates. The maximum throw measured by Papanikolaou *et al*. (2013) is 9.7 m, which gives a Holocene slip of 11 m and a slip rate of 0.73 mm/yr. The minimum throw is measured by this study is 7.53 m, giving a Holocene slip of 8.31 m and thus a slip rate of 0.55 mm/yr.

This analysis shows that the lower dip of the fault results in a higher annual rate of occurrence (i.e., earthquakes will occur more frequently) than the steeper fault dip (Fig. 12a). For example, the expected recurrence interval for M>5.5 earthquakes would be 106 years for the 31° dipping fault and 245 years for the 67° dipping fault. There are no instrumentally-recorded earthquakes with M>5.5 that have been located close enough to the Sparta Fault for it to be the source fault, in other words the fault has not experienced a M>5.5 earthquake in at least 70 years.

In seismic hazard assessment, Ground Motion Prediction Equations (GMPE's) are used to calculate the expected ground shaking, and an input into these equations is some measure of the distance between the earthquake source and site of interest. For example, the distance from the site to the surface projection of the rupture/fault (Joyner-Boore distance, R_{JB}) or the distance from the site to the rupture/fault plane (R_{RUP}). For this study, how R_{RUP} for Sparta city would be different depending on the dip of the fault plane can be calculated. The structural measurements taken closest to the city of Sparta give an average dip of 61° (localities 12 and 18-22), but within a few kilometers to the north, the dip of the fault becomes much shallower, as low as 31°. When R_{RUP} is calculated for these dip values (Fig. 12b), it is clear that the R_{RUP} for the steeper dip is 1.5 times greater than for the shallow dip. The relationship between R_{RUP} and ground shaking depends on the empirical equation used, but it is generally non-linear. Therefore mis-estimating R_{RUP} because of uncertainties about fault dip may more than double the calculated expected ground shaking.

As a consequence, the Sparta region is going to be possibly affected by the next earthquake and is evaluated in terms of time dependent and independent probabilities (Papanikolaou *et al.*, 2013), the former ranges from 1.69% to 4.76% over the next three decades and the latter is 1.66%. The recurrence interval is also calculated as 1792 ± 458 years. In the light of the geological and geomorphological evidence, when an earthquake occurs, the central localities of the Sparta region will be highly affected because of low dip angle fault (Fig. 12).

Holocene Activity of the Sparta Fault

A new topographic profile across a Holocene fault scarp identified along the northern section of the fault is interpreted as having a post-glacial throw of 7.53 ± 1.51 m (Fig. 6). This offset equates to a throw rate of 0.50 ± 0.14 mm/yr if the age of the scarp is taken as 15 ± 3 kyrs (e.g., Benedetti *et al*., 2002; Papanikolaou *et al*., 2013). This new site indicates that the northern section of the Sparta fault should be considered as being active in the Holocene and has a slip rate almost twice that previously suggested by Papanikolaou *et al*. (2013). Additionally, the post-glacial throw is of comparable magnitude to the measurements made in the southern section (e.g., Papanikolaou *et al*., 2013), which is slightly surprising given the lower inferred activity and proximity to the northern tip of the fault. However, the orientation of the fault at this point is oblique (~270°) compared to the overall fault strike (~320°). Other studies on normal faults (e.g., Faure Walker *et al.*, 2009; Wilkinson *et al.*, 2015; Mildon *et al.*, 2016; Iezzi *et al.*, 2018) show that Holocene throw tends to increase in fault bends (aka mis-orientated sections), hence the throw measured may be higher than expected due to the local fault geometry.

Yet, these new data are consistent with the results of Benedetti *et al.* (2002) and Papanikolaou *et al*. (2013), whose work indicates that the slip-rate at Anogia is 0.5-0.6 mm/yr. Anogia is located towards the southern tip of the fault zone suggesting that the Sparta Fault rapidly gains offset along strike. As a result, the Holocene along-strike activity of the fault can be estimated

(Fig. 13). This inferred throw profile indicates that the present-day maximum throw rate on the fault is in the order of 0.8 mm/yr.

Quaternary activity of the Sparta Fault constrained by the fluvial response to active faulting

While the well-exposed post-glacial fault scarp can give insights into the Holocene activity of the fault, alternative methods are required to infer the older Quaternary development of the Sparta Fault. This can be realised through analysis of the river profiles crossing the fault, as the long-term evolution of the river channels is directly affected by the uplift (i.e., throw) on the fault.

Significantly, three sets of knickpoints can be identified along rivers flowing across the footwall of the Sparta Fault; a vertical-step knickpoint and two generations of slope-break knickpoints. Where present, the vertical-step knickpoint is located at or slightly upstream of a lithological boundary, most frequently this is the contact between the basement Arna unit and the overlying Mani unit typically composed of thick bedded dolomites or limestones. This association and knickpoint morphology indicate that these knickpoints are likely to be fixed at these locations owing to the lithological strength contrast between these bedrock lithologies.

By contrast, the slope-break knickpoints are located upstream of the fault but are not associated with major lithological boundaries. This observation combined with the increased steepness downstream (Fig. 10D), scaling between the catchment area and upstream distance of the knickpoint (Fig. 11A) demonstrate that these knickpoints have migrated upstream and represent the upstream migration of a transient wave of incision along the river networks caused by a relative base-level fall. Given the location of the knickpoints along an active fault, then changes to the slip-rate along the fault are the most likely driver of incision with the two sets of knickpoints indicating two different events.

The higher knickpoint represents an earlier phase of incision, though it is notable that 73% of the higher knickpoints are located at catchments areas of ≤ 1 km^2 (Fig. 11B). This suggests that these knickpoints are at or close to the threshold drainage area for knickpoint migration (c.f. Crosby and Whipple, 2006). Therefore, it is likely that these knickpoints represent an early phase of incision along the fault that is now close to having completely migrated through the system. The early phase of base-level lowering may be the result of the onset of normal faulting along the fault (c.f., Whittaker and Walker, 2015; Roda-Boluda and Whittaker, 2017). Knickpoints would have formed along all rivers draining the footwall but in the southernmost rivers the wave of incision has already propagated through the entire channel. By contrast, the higher knickpoints present in the north indicate that this incision has not yet fully migrated through the system or has become pinned at low drainage areas in these small catchments. This hypothesis is supported by the presence of lower relief areas in the north, potentially the remnants of the pre-uplift topography, and is consistent with knickpoints migrating faster in catchments experiencing higher slip rates (i.e., in the south; Boulton and Whittaker, 2009; Whittaker and Boulton, 2012).

By contrast, the lower slope-break knickpoints are all located at catchments areas > 1 km^2 and are still found at a range of positions through the catchments indicating that these features represent a more recent change in slip rate, which may have been driven by fault linkage / interactions or by a regionally driven acceleration of the fault. Based upon the k_{sn} ratio of stream segments above and below these lower knickpoints, the change in slip rate would have been in the order of ~ 2 times. Interestingly, the along strike pattern of knickpoints (Fig. 10) is markedly different to other studies investigating transient incision along normal faults (i.e., (Boulton and Whittaker, 2009; Kent *et al.*, 2017; He *et al.*, 2018). These studies generally report lower knickpoints near both fault tips, and higher knickpoints at fault segment boundaries, interpreted to be the result of fault linkage of shorter faults driving higher throw rates where fault linkage has occurred. Therefore, the trend of knickpoints decreasing with height northwards along the Sparta Fault would be more compatible with a generalised acceleration in base-level lowering (e.g., Miller *et al.*, 2012; Olivetti *et al.*, 2012; Roda-Boluda and Whittaker, 2017), perhaps the result of an increase in strain rates across the Peloponnese causing the slip-rate on the fault to increase. This interpretation is favoured over a regional base-level fall as the overall pattern of knickpoint elevation follows the present-day throw distribution indicating a causative link. Though, the limited age control on local marine terrace sequences suggests constant regional uplift during the Quaternary (Kourampas, 2001; Athanassas and Fountoulis, 2013; Karymbalis *et al.*, 2022).

Interestingly, both sets of knickpoints show a marked decrease in height (Fig. 10B) above the active fault along strike, with knickpoints higher in the catchments in the south compared the north. As the vertical component of knickpoint celerity is controlled by the slip rate on the fault (Whittaker and Boulton, 2012), this suggests that over long timescales the fault has a highly asymmetrical throw profile with much higher slip rates in the south than in the north. The asymmetric pattern is consistent with the field observations on the Holocene slip from the post-glacial fault scarp, which deviates from a symmetrical profile more commonly described for normal fault. If this is the case, then these data suggest that the Sparta Fault has an asymmetrical throw profile that has persisted on the time-scales of the fluvial response, which is on the order of ~ 10^6 years. This is unusual as other examples of such asymmetry are generally associated with complex fault arrays; however, there is no topographic evidence suggesting that the Sparta Fault extends much further to the south than it's topographic expression indicates, and there is no significant fault shown in the recent seismotectonic atlas (Kassaras *et al.*, 2020). Therefore, the Sparta Fault represents an intriguing example of fault geometry and behaviour that is inconsistent with existing models, and as such would justify further investigation.

Conclusion

The Sparta Fault has been examined in terms of its geometry, post-glacial throw and steepness of the river channels by using fieldwork measurements, DEM analysis of the fluvial geomorphology, and seismic hazard assessment. These analyses demonstrate for the first time that the northern section of the fault, long considered to be minimally active or inactive does in fact exhibit > 7 m of post-glacial throw equating to a slip rate of ~ 0.5 mm/yr.

This interpretation is supported by an expanded analysis of rivers crossing the fault, these rivers exhibit up to two slope-break knickpoints along the whole range of the fault that are interpreted as representing the initial of faulting and an acceleration of slip-rate along the fault caused by either a regional change in strain rate or fault-linkage. Furthermore, the height of the knickpoints above the fault echo the general pattern seen in the post-glacial fault scarp of higher values in the south and lower in the north. These two lines of evidence; therefore, suggest that the Sparta Fault has an asymmetrical throw profile.

Additionally, these data and measurements on the dip angle of the fault are used to model two seismic hazard scenarios for the city of Sparta. This demonstrates that the dip of the fault will significantly affect the recurrence interval and as a result when an earthquake occurs, the central localities of the Sparta region will be highly affected because of low dip angle fault in this area. These considerations around varying fault geometries have previously not been taken into account and highlight the need for further seismic hazard assessment in this populous region.

Acknowledgements: We thank two anonymous reviewers for comments that have improved this work.

Funding Information: This research was undertaken as part of a ResM Scholarship to Çağatay Çal at the University of Plymouth, funded by Republic of Türkiye Ministry of National Education.

Data Availability: All data generated or analysed during this study are included in this published article (and its supplementary information files) or are publicly available through the stated websites and organisations.

REFERENCES

Agostini, S., Doglioni, C., Innocenti, F., Manetti, P., Tonarini, S., 2010. On the geodynamics of the Aegean rift. Tectonophysics 488, 7–21. https://doi.org/10.1016/j.tecto.2009.07.025.

Allmendinger, R.W., Cardozo, N.C., Fisher, D., 2013. Structural Geology Algorithms: Vectors and Tensors. Cambridge University Press, Cambridge, England, 289 pp.

Armijo, R., Lyon-Caen, H. and Papanastassiou, D. 1991. A possible normal-fault rupture for the 464 BC Sparta earthquake. *Nature*, **351**, 137–139, https://doi.org/10.1038/351137a0.

Athanassas, C. and Fountoulis, I. 2013. Quaternary neotectonic configuration of the southwestern Peloponnese, Greece, based on luminescence ages of marine terraces. *Journal of Earth Science*, **24**, 410–427, https://doi.org/10.1007/s12583-013-0334-1.

BASMENJI, M., SANÇAR, T., DİKBAŞ, A., BOULTON, S. and AKYÜZ, H. 2021. Tectonic geomorphology of the Yatağan Fault (Muğla, SW Turkey): implications for quantifying vertical slip rates along active normal faults. Turkish Journal of Earth Sciences, 30, 460–488, https://doi.org/10.3906/yer-2010-11.

Benedetti, L., Finkel, R., et al. 2002. Post-glacial slip history of the Sparta fault (Greece) determined by 36Cl cosmogenic dating: Evidence for non-periodic earthquakes. *Geophysical Research Letters*, **29**, 1–4, https://doi.org/10.1029/2001gl014510.

Bishop, P., Hoey, T.B., Jansen, J.D. and Lexartza Artza, I. 2005. Knickpoint recession rate and catchment area: The case of uplifted rivers in Eastern Scotland. *Earth Surface Processes and Landforms*, **30**, 767–778, https://doi.org/10.1002/esp.1191.

Boulton, S.J. and Whittaker, A.C. 2009. Quantifying the slip rates, spatial distribution and evolution of active normal faults from geomorphic analysis: Field examples from an oblique-extensional graben, southern Turkey. *Geomorphology*, **104**, 299–316.

Bubeck, A., Wilkinson, M., Roberts, G. P., Cowie, P. A., McCaffrey, K. J. W., Phillips, R., & Sammonds, P. (2015). The tectonic geomorphology of bedrock scarps on active normal faults in the Italian Apennines mapped using combined ground penetrating radar and terrestrial laser scanning. Geomorphology, 237, 38-51.

Cardozo N., and Allmendinger, 2013. Spherical projections with OSXStereonet. Computers and Geosciences, 51, 193-205.

Cowie, P.A., Phillips, R.J., et al. 2017. Orogen-scale uplift in the central Italian Apennines drives episodic behaviour of earthquake faults. *Scientific Reports*, **7**, 44858, https://doi.org/10.1038/srep44858.

Crosby, B.T. and Whipple, K.X. 2006. Knickpoint initiation and distribution within fluvial networks: 236 waterfalls in the Waipaoa River, North Island, New Zealand. *Geomorphology*, **82**, 16–38, https://doi.org/10.1016/j.geomorph.2005.08.023.

DiBiase, R.A., Whipple, K.X., Heimsath, A.M. and Ouimet, W.B. 2010. Landscape form and millennial erosion rates in the San Gabriel Mountains, CA. *Earth and Planetary Science Letters*, **289**, 134–144, https://doi.org/10.1016/j.epsl.2009.10.036.

Flint, J.J. 1974. Stream gradient as a function of order, magnitude, and discharge. *Water Resources Research*, **10**, 969–973, https://doi.org/10.1029/WR010i005p00969.

Forte, A.M. and Whipple, K.X. 2019. Short communication: The Topographic Analysis Kit (TAK) for TopoToolbox. *Earth Surface Dynamics*, **7**, 87–95, https://doi.org/10.5194/esurf-7-87-2019.

Gallen, S.F. and Wegmann, K.W. 2017. River profile response to normal fault growth and linkage: an example from the Hellenic forearc of south-central Crete, Greece. Earth Surf. Dynam., 5, 161–186, https://doi.org/10.5194/esurf-5-161-2017.

Gürer, D., Granot, R. and van Hinsbergen, D. 2022. Plate tectonic chain reaction revealed by noise in the Cretaceous quiet zone. *Nature Geoscience*, **15**, https://doi.org/10.1038/s41561-022-00893-7.

Haviv, I., Enzel, Y., Whipple, K.X., Zilberman, E., Matmon, A., Stone, J. and Fifield, K.L. 2010. Evolution of vertical knickpoints (waterfalls) with resistant caprock: Insights from numerical modeling. *Journal of Geophysical Research: Earth Surface*, **115**, 1–22, https://doi.org/10.1029/2008JF001187.

He, C., Cheng, Y., Rao, G., Chen, P., Hu, J., Yu, Y. and Yao, Q. 2018. Geomorphological signatures of the evolution of active normal faults along the Langshan Mountains, North China. *Geodinamica Acta*, **30**, 163–182, https://doi.org/10.1080/09853111.2018.1458935.

Howard, A.D. and Kerby, G. 1983. Howard-Kerby_GSAB_83.pdf. *Geological Society of America Bulletin*, **94**, 739–752.

Howard, A.D., Dietrich, W.E. and Seidl, M.A. 1994. Modeling fluvial erosion on regional to continental scales. *Journal of Geophysical Research*, **99**, https://doi.org/10.1029/94jb00744.

Hughes, P.D., Gibbard, P.L. and Woodward, J.C. 2005. Quaternary glacial records in mountain regions: A formal stratigraphical approach. *Episodes*, **28**, 85–92, https://doi.org/10.18814/epiiugs/2005/v28i2/002.

Iezzi, F., Mildon, Z., Walker, J.F., Roberts, G., Goodall, H., Wilkinson, M. and Robertson, J. 2018. Coseismic Throw Variation Across Along-Strike Bends on Active Normal Faults: Implications for Displacement Versus Length Scaling of Earthquake Ruptures. *Journal of Geophysical Research: Solid Earth*, **123**, 9817–9841, https://doi.org/10.1029/2018JB016732.

Iezzi, F., Roberts, G., Walker, J.F. and Papanikolaou, I. 2019. Occurrence of partial and total coseismic ruptures of segmented normal fault systems: Insights from the Central Apennines, Italy. *Journal of Structural Geology*, **126**, 83–99, https://doi.org/10.1016/j.jsg.2019.05.003.

Jolivet, L. and Brun, J.P. 2010. Cenozoic geodynamic evolution of the Aegean. *International Journal of Earth Sciences*, **99**, 109–138, https://doi.org/10.1007/s00531-008-0366-4.

Karymbalis, E., Tsanakas, K., Tsodoulos, I., Gaki-Papanastassiou, K., Papanastassiou, D., Batzakis, D.-V. and Stamoulis, K. 2022. Late Quaternary Marine Terraces and Tectonic Uplift Rates of the Broader Neapolis Area (SE Peloponnese, Greece). *Journal of Marine Science and Engineering*, **10**, 99, https://doi.org/10.3390/jmse10010099.

Kassaras, I., Kapetanidis, V., et al. 2020. The New Seismotectonic Atlas of Greece (v1.0) and Its Implementation. *Geosciences*, **10**, 447, https://doi.org/10.3390/geosciences10110447.

Kent, E., Boulton, S.J., Whittaker, A.C., Stewart, I.S. and Cihat Alçiçek, M. 2017. Normal fault growth and linkage in the Gediz (Alaşehir) Graben, Western Turkey, revealed by transient river long-profiles and slope-break knickpoints. *Earth Surface Processes and Landforms*, **42**, https://doi.org/10.1002/esp.4049.

Kirby, E. and Whipple, K. 2001. Quantifying differential rock-uplift rates via stream profile analysis. *Geology*, **29**, 415–418, https://doi.org/10.1130/0091-7613(2001)029<0415:QDRURV>2.0.CO;2.

Kirby, E. and Whipple, K.X. 2012. Expression of active tectonics in erosional landscapes. *Journal of Structural Geology*, **44**, 54–75, https://doi.org/10.1016/j.jsg.2012.07.009.

Kourampas, N. (2001) 'Plio-Quaternary sedimentation and geomorphology within an Kourampas, N. 2001. Plio-Quaternary sedimentation and geomorphology within an active fore-arc : Messenia and Eastern Lakonia Peninsulae, Southern Peloponnese, Greece.

Koutsovitis, P., Magganas, A., Ntaflos, T., Koukouzas, N., Rassios, A.E., Soukis, K., 2020. Petrogenetic constraints on the origin and formation of the Hellenic Triassic rift-related lavas. Lithos 368–369, 105604. https://doi.org/10.1016/j.lithos.2020.105604

Liu, Z., Han, L., Boulton, S.J., Wu, T. and Guo, J. 2020. Quantifying the transient landscape response to active faulting using fluvial geomorphic analysis in the Qianhe Graben on the southwest margin of Ordos, China. *Geomorphology*, **351**, 106974, https://doi.org/10.1016/j.geomorph.2019.106974.

Lyon-Caen, H. 1988. The 1986 Kalamata (south Peloponnesus) earthquake: detailed study of a normal fault, evidences for east-west extension in the Hellenic arc. *Journal of Geophysical Research*, **93**, https://doi.org/10.1029/jb093ib12p14967.

Lyon-Caen, H., Armijo, R., et al. 1988. The 1986 Kalamata (South Peloponnesus) Earthquake: Detailed study of a normal fault, evidences for east-west extension in the Hellenic Arc. *Journal of Geophysical Research: Solid Earth*, **93**, 14967–15000, https://doi.org/10.1029/JB093iB12p14967.

Marliyani, G.I., Arrowsmith, J.R. and Whipple, K.X. 2016. Characterization of slow slip rate faults in humid areas: Cimandiri fault zone, Indonesia. *Journal of Geophysical Research: Earth Surface*, **121**, 2287–2308, https://doi.org/10.1002/2016JF003846.

MASTRONUZZI, G., SANSÒ, P. and STAMATOPOULOS, L. 1994. The glacial landforms of the Peloponnisos (Greece). *The glacial landforms of the Peloponnisos (Greece)*, **101**, 77–86.

McClusky, S., Balassanian, S., et al. 2000. Global Positioning System constraints on plate kinematics and dynamics in the eastern Mediterranean and Caucasus. *Journal of Geophysical Research: Solid Earth*, **105**, 5695–5719, https://doi.org/10.1029/1999JB900351.

Mechernich, S., Reicherter, K., Deligiannakis, G. and Papanikolaou, I. 2023. Tectonic geomorphology of active faults in Eastern Crete (Greece) with slip rates and earthquake history from cosmogenic 36Cl dating of the Lastros and Orno faults. *Quaternary International*, **651**, 77–91.

Mildon, Z.K., Roberts, G.P., Walker, J.P.F., Wedmore, L.N. and McCaffrey, K.J. 2016. Active normal faulting during the 1997 seismic sequence in Colfiorito, Umbria: Did slip propagate to the surface? *Journal of Structural Geology*, **91**, 102–113.

Miller, S.R., Baldwin, S.L. and Fitzgerald, P.G. 2012. Transient fluvial incision and active surface uplift in the Woodlark Rift of eastern Papua New Guinea. *Lithosphere*, **4**, 131–149, https://doi.org/10.1130/L135.1.

Olivetti, V., Cyr, A.J., Molin, P., Faccenna, C. and Granger, D.E. 2012. Uplift history of the Sila Massif, southern Italy, deciphered from cosmogenic10Be erosion rates and river longitudinal profile analysis. *Tectonics*, **31**, n/a-n/a, https://doi.org/10.1029/2011tc003037.

Pace, B., Visini, F. and Peruzza, L. 2016. FiSH: MATLAB tools to turn fault data into seismic-hazard models. *Seismological Research Letters*, **87**, 374–386.

Papanastassiou, D., Gaki-Papanastassiou, K. and Maroukian, H. 2005. Recognition of past earthquakes along the Sparta fault (Peloponnesus, southern Greece) during the Holocene, by combining results of different dating techniques. *Journal of Geodynamics*, **40**, 189–199, https://doi.org/10.1016/j.jog.2005.07.015.

Papanikolaou, D., Lykousis, V., Chronis, G. and Pavlakis, P. 1988. A comparative study of neotectonic basins across the Hellenic arc: the Messiniakos, Argolikos, Saronikos and Southern Evoikos Gulfs. *Basin Research*, **1**, 167–176, https://doi.org/10.1111/j.1365-2117.1988.tb00013.x.

Papanikolaou, D.J. and Royden, L.H. 2007. Disruption of the Hellenic arc: Late Miocene extensional detachment faults and steep Pliocene-Quaternary normal faults - Or what happened at Corinth? *Tectonics*, **26**, 1–16, https://doi.org/10.1029/2006TC002007.

Papanikolaou, I.D., Roberts, G.P., Deligiannakis, G., Sakellariou, A. and Vassilakis, E. 2013. The sparta fault, southern Greece: From segmentation and tectonic geomorphology to seismic hazard mapping and time dependent probabilities. *Tectonophysics*, **597–598**, 85–105, https://doi.org/10.1016/j.tecto.2012.08.031.

Paul R. Bierman; David R. Montgomery. 2020. *Key Concepts in Geomorphology*.

Pe-Piper, G. and PIPER, D.W. 1985. Late-Cenozoic clays and climatic change in the post-orogenic Lakonia Graben, southern Greece. *Neues Jahrbuch für Mineralogie. Abhandlungen*, **151**, 301–313.

Piper D.J.W. 2006. Sedimentology and tectonic setting of the Pindos Flysch of the Peloponnese, Greece. Geological Society, London, Special Publications, 260, 493–505, https://doi.org/10.1144/GSL.SP.2006.260.01.20.

Piper, D.J., Pe-Piper, G., Kontopoulos, N. and Panagos, A.G. 1982. Plio-Pleistocene sedimentation in the western Lakonia graben, Greece. *Neues Jahrbuch für Geologie und Paläontologie-Monatshefte*, 679–691.

Pope, R.J.J. and Wilkinson, K.N. 2005. Reconciling the roles of climate and tectonics in Late Quaternary fan development on the Spartan piedmont, Greece. *Geological Society Special Publication*, **251**, 133–152, https://doi.org/10.1144/GSL.SP.2005.251.01.10.

Pope, R.J.J., Wilkinson, K.N. and Millington, A.C. 2003. Human and climatic impact on late quaternary deposition in the sparta basin piedmont: Evidence from alluvial fan systems. *Geoarchaeology*, **18**, 685–724, https://doi.org/10.1002/gea.10089.

Reilinger, R., McClusky, S., et al. 2006. GPS constraints on continental deformation in the Africa-Arabia-Eurasia continental collision zone and implications for the dynamics of plate interactions. *Journal of Geophysical Research: Solid Earth*, **111**.

Reilinger, R.E., McClusky, S.C., et al. 1997. Global Positioning System measurements of present-day crustal movements in the Arabia-Africa-Eurasia plate collision zone. *Journal of Geophysical Research: Solid Earth*, **102**, 9983–9999, https://doi.org/10.1029/96jb03736.

Roda-Boluda, D.C. and Whittaker, A.C. 2017. Structural and geomorphological constraints on active normal faulting and landscape evolution in Calabria, Italy. *Journal of the Geological Society*, **174**, 701–720, https://doi.org/10.1144/jgs2016-097.

Schlagenhauf, A., Manighetti, I., Benedetti, L., Gaudemer, Y., Finkel, R., Malavieille, J. and Pou, K. 2011. Earthquake supercycles in Central Italy, inferred from 36Cl exposure dating. *Earth and Planetary Science Letters*, **307**, 487–500.

Schwanghart, W. and Scherler, D. 2014. Short Communication: TopoToolbox 2 - MATLAB-based software for topographic analysis and modeling in Earth surface sciences. *Earth Surface Dynamics*, **2**, 1–7, https://doi.org/10.5194/esurf-2-1-2014.

Schwanghart, W., Scherler, D. 2014. TopoToolbox 2 – MATLAB-based software for topographic analysis and modeling in Earth surface sciences. *Earth Surface Dynamics*, **2**, https://doi.org/10.5194/esurf-2-1-2014].

Tucker, G.E. and Whipple, K.X. 2002. Topographic outcomes predicted by stream erosion models: Sensitivity analysis and intermodel comparison. *Journal of Geophysical Research: Solid Earth*, **107**, ETG 1-1-ETG 1-16, https://doi.org/10.1029/2001jb000162.

Walker, J.F., Roberts, G.P., Cowie, P.A., Papanikolaou, I.D., Sammonds, P.R., Michetti, A.M. and Phillips, R.J. 2009. Horizontal strain-rates and throw-rates across breached relay zones, central Italy: Implications for the preservation of throw deficits at points of normal fault linkage. *Journal of Structural Geology*, **31**, 1145–1160.

Whipple, K.X. 2001. Fluvial landscape response time: How plausible is steady-state denudation? *American Journal of Science*, **301**, 313–325, https://doi.org/10.2475/ajs.301.4-5.313.

Whipple, K.X. 2004. Bedrock rivers and the geomorphology of active orogens. *Annual Review of Earth and Planetary Sciences*, **32**, 151–185, https://doi.org/10.1146/annurev.earth.32.101802.120356.

Whipple, K.X. and Tucker, G.E. 1999. Dynamics of the stream-power river incision model: Implications for height limits of mountain ranges, landscape response timescales, and research needs. *Journal of Geophysical Research: Solid Earth*, **104**, 17661–17674, https://doi.org/10.1029/1999JB900120.

Whittaker, A.C. and Boulton, S.J. 2012. Tectonic and climatic controls on knickpoint retreat rates and landscape response times. *Journal of Geophysical Research: Earth Surface*, **117**, 1–19, https://doi.org/10.1029/2011JF002157.

Whittaker, A.C. and Walker, A.S. 2015. Geomorphic constraints on fault throw rates and linkage times: Examples from the Northern Gulf of Evia, Greece. *Journal of Geophysical Research: Earth Surface*, **120**, 137–158, https://doi.org/10.1002/2014jf003318.

Whittaker, A.C., Cowie, P.A., Attal, M., Tucker, G.E. and Roberts, G.P. 2007. Bedrock channel adjustment to tectonic forcing: Implications for predicting river incision rates. *Geology*, **35**, 103–106, https://doi.org/10.1130/G23106A.1.

Wilkinson, M., Roberts, G.P., et al. 2015. Slip distributions on active normal faults measured from LiDAR and field mapping of geomorphic offsets: an example from L'Aquila, Italy, and implications for modelling seismic moment release. *Geomorphology*, **237**, 130–141.

Wobus, C.W., Hodges, K. V. and Whipple, K.X. 2003. Has focused denudation sustained active thrusting at the Himalayan topographic front? *Geology*, **31**, 861–864, https://doi.org/10.1130/G19730.1.

Wobus, C.W., Crosby, B.T. and Whipple, K.X. 2006. Hanging valleys in fluvial systems: Controls on occurrence and implications for landscape evolution. *Journal of Geophysical Research: Earth Surface*, **111**, 1–14, https://doi.org/10.1029/2005JF000406.

Figure/Table Captions

Locality	UTM_x	UTM_y	Strike	Dip direct	Dip	# plane da	Plunge	Trend	# slip vect
1	628824	4091015	298.1212	28.12122	65.49384	2	33	79	1
2	628492	4091145	317.676	47.67602	52.81658	6	35.39801	46.72958	7
3	618660	4108254	314.0848	44.08484	53.18382	6	55.51332	45.50982	2
4	618515	4108430	329.8219	59.82193	52.41956	6	59	52.4	1
5	618143	4109565	323	53	31	1	N/A	N/A	N/A
6	617005	4112864	297	27	41.8914	2	N/A	N/A	N/A
7	627175	4094666	9.595366	99.59537	71.4836	2	N/A	N/A	N/A
8	627184	4094719	4.23842	94.23842	66.9538	8	100.7869	65.92083	7
9	627132	4095666	328.2298	58.22981	51.16487	9	96.2	43.9	1
10	625773	4098728	337.5797	67.57968	58.15334	12	65.50995	56.86658	8
11	625734	4098817	341.7466	71.74663	58.38809	7	76.05193	56.0161	4
12	623300	4102290	325.7859	55.78587	59.42756	10	45	58.7	1
13	610654	4122885	4.326951	94.32695	50.31808	3	100.0212	50.51713	2
14	610234	4123850	336.1679	66.16789	34.45086	6	43.12393	32.61744	9
15	608326	4125475	257.9457	347.9457	63.63225	54	8.954287	61.07038	13
16	608364	4125469	272	2	62	1	N/A	N/A	N/A
17	602724	4130439	339.206	69.20601	42.14861	11	73.2353	42.26707	8
18	623464	4102058	356.8531	86.85313	65.94019	8	N/A	N/A	N/A
19	623453	4102088	333.9602	63.96017	64.0167	13	68	64	1
20	623425	4102129	316.3344	46.33443	60.66584	3	N/A	N/A	N/A
21	623397	4102182	321.9893	51.98933	60.53637	3	N/A	N/A	N/A
22	623351	4102228	313.3197	43.31967	58.6966	20	39.6891	57.27963	12
23	626198	4097314	324	54	55	1	N/A	N/A	N/A

Table 1. Summary structural data for the post-glacial fault scarp, field data used to calculate the mean values is available in the supplemental information.

River Num	Distance a	Active fau	Total river	Total catch	Catchmen	Knickpoin	Knickpoin	Knick-poi	KP height	K_{sn} upstrea	K_{sn} downs	K_{sn} ratio
3*	7.82	260	6785.61	5.00647	1.264131	1581.61	5204	1148	888	60.48	107.57	1.7786045
4*	9.37	317	5294	15.08696	11.66333	1140	4154	1878	1561	49.65	177.54	3.5758308
6*	12.99	326	7123	12.47965	0.974275	1482	5641	1227	901	104.47	125.63	1.2025462
7	15.15	296	7131	12.47965	3.474956	3725	3406	799	503	129.15	179.11	1.386837
8	18.65	300	7465.8	12.48234	8.603369	3883	3582.8	860	560	109.27	172.39	1.5776517
8*	18.65	300	7465.8	12.48234	1.10222	856	6609.8	1302	1002	97.31	109.27	1.1229062
9*	19.91	345	5858.8	11.71594	0.246697	603	5255.8	1328	983	85.81	133.14	1.5515674
9	19.91	345	5858.8	11.71594	2.238023	1854	4004.8	1011	666	133.14	206.7	1.5525011
10	22.79	447	10127.9	36.55011	29.29949	6763	3364.9	764	317	81.67	197.16	2.4141055
11	25.6	607	3330.3	2.969431	1.927736	2208	1122.3	994	387	133.28	169.15	1.2691327
12*	27.37	545	4456.5	5.9727	2.325363	932	3524.5	1353	808	60.27	220.53	3.6590343
13	30.54	454	5808.4	6.995624	6.197179	4392	1416.4	966	512	70.48	262.44	3.7236095
13*	30.54	454	5808.4	6.995624	0.176468	179	5629.4	1426	972	50.92	70.47	1.3839356
14	32.28	499	4561.8	4.985911	4.622123	3452	1109.8	700	201	113.66	177.83	1.5645786
14*	32.28	499	4561.8	4.985911	0.331228	512	4049.8	1305	806	46.54	113.66	2.4422003
15	33.42	530	3515.1	4.839834	4.135879	2693	822.1	687	157	102.88	161.37	1.5685264
15*	33.42	530	3515.1	4.839834	0.1863	458	3057.1	1134	604	85.79	102.88	1.1992074
16	33.91	597	3316.9	4.418457	3.796096	2320.48	996.42	743	146	121.61	134.21	1.1036099
16*	33.91	597	3316.9	4.418457	0.248229	95.48	3221.42	1347	750	56.99	121.62	1
17*	39.21	733	2705.9	1.869765	0.523657	697	2008.9	1217	484	64.04	129.16	2.0168645
18*	39.9	699	3282.4	3.159689	0.739325	623	2659.4	1260	561	16.7	157.15	9.4101796

Table 2: Data extracted for rivers of the study area; higher elevation knickpoints indicated by *.

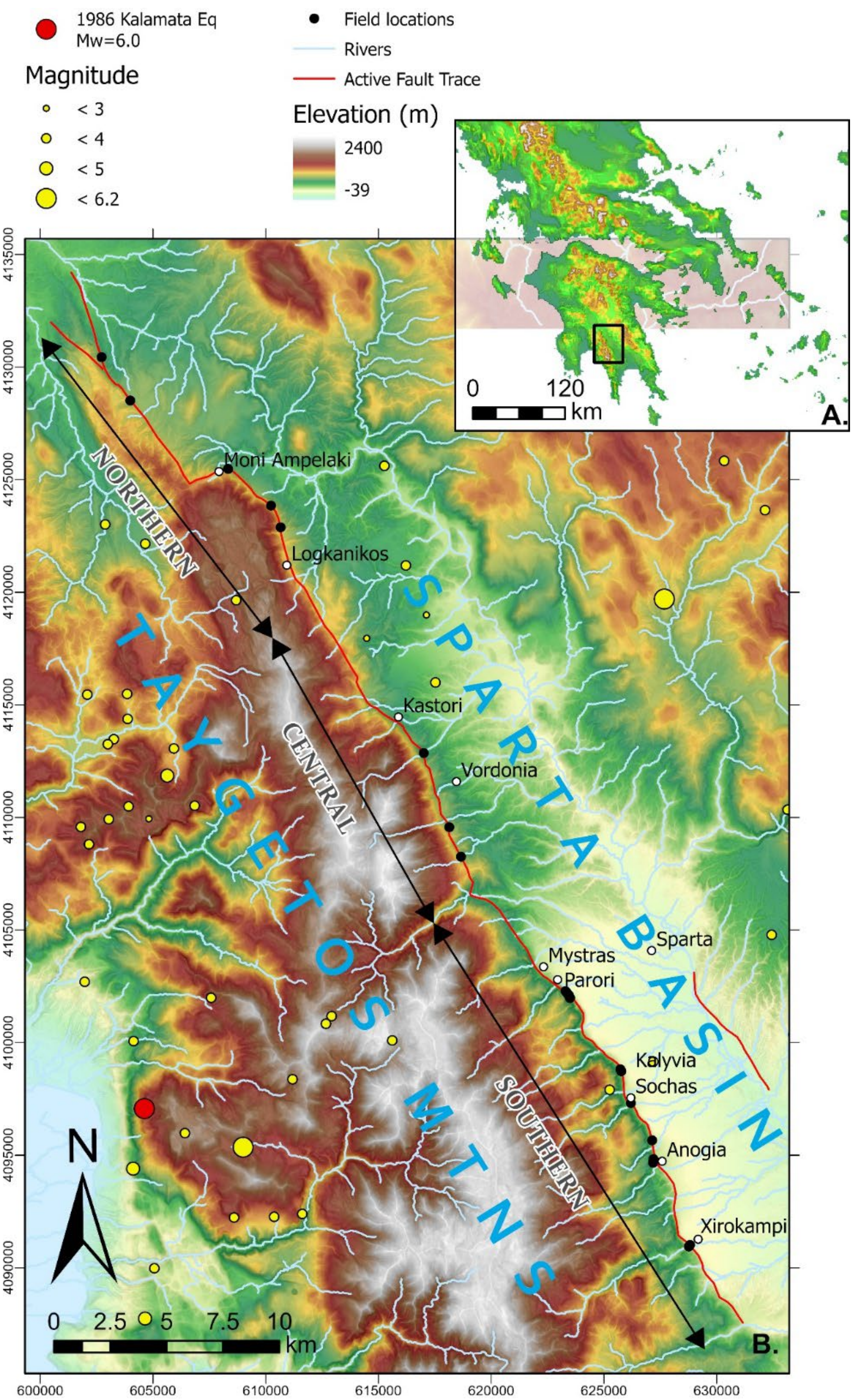

Figure 1: A. GTOPO 1 km DEM showing regional context of the study area in southern Greece; B. Physiographic map of the Sparta region with key locations mentioned in the text shown and the recent seismicity of region from the USGS catalogue covering the period from September 1949 to March 2023 (https://earthquake.usgs.gov/earthquakes/) including the 1986 Kalamata earthquakes. The DEM is the 30 m ALOS World3D30 DEM ©JAXA projected in UTM Zone 34N.

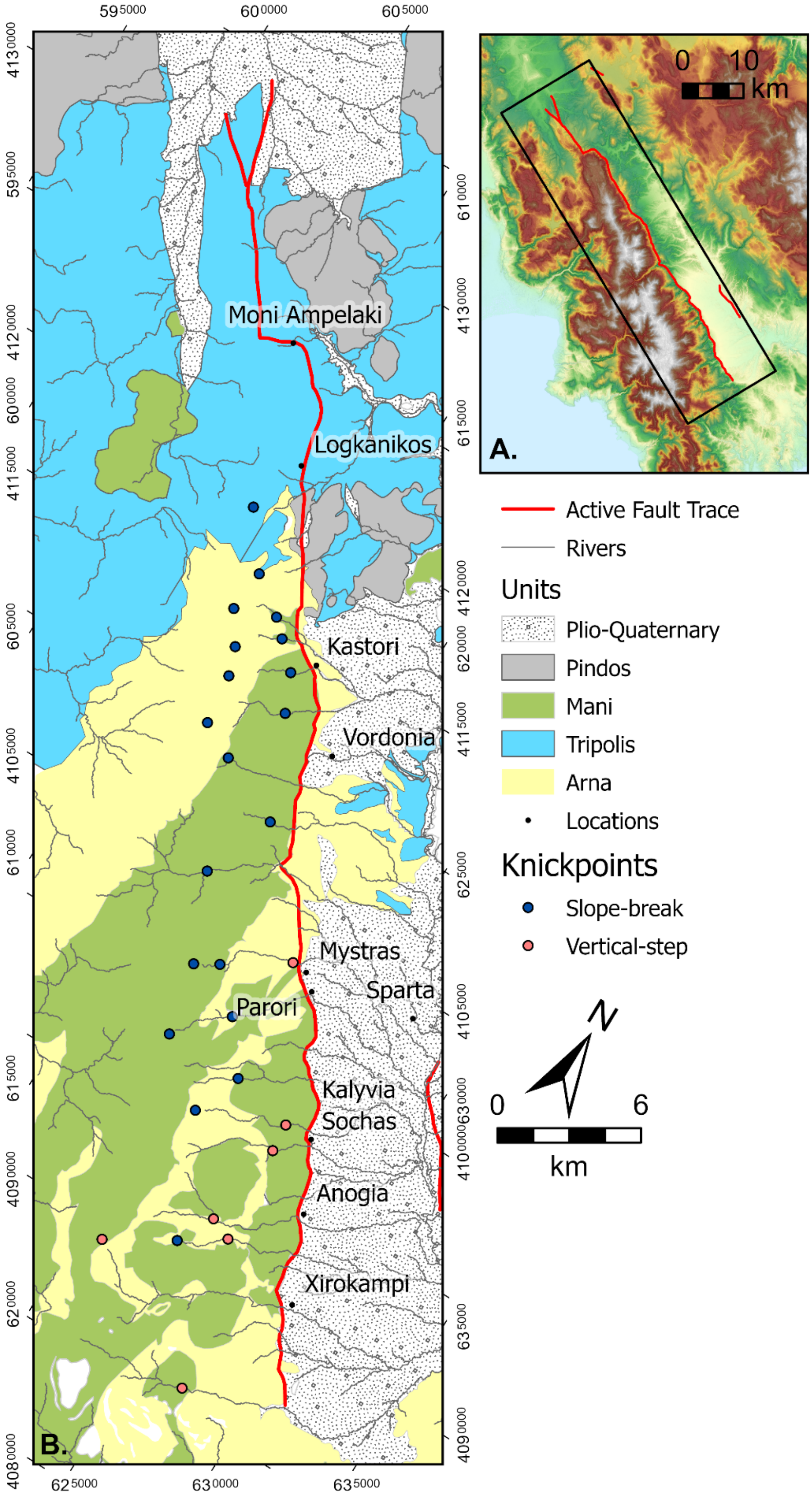

Figure 2. A) Inset map showing extent covered by B) simplified geological map of the study area adapted from Papanikolaou et al. (2013).

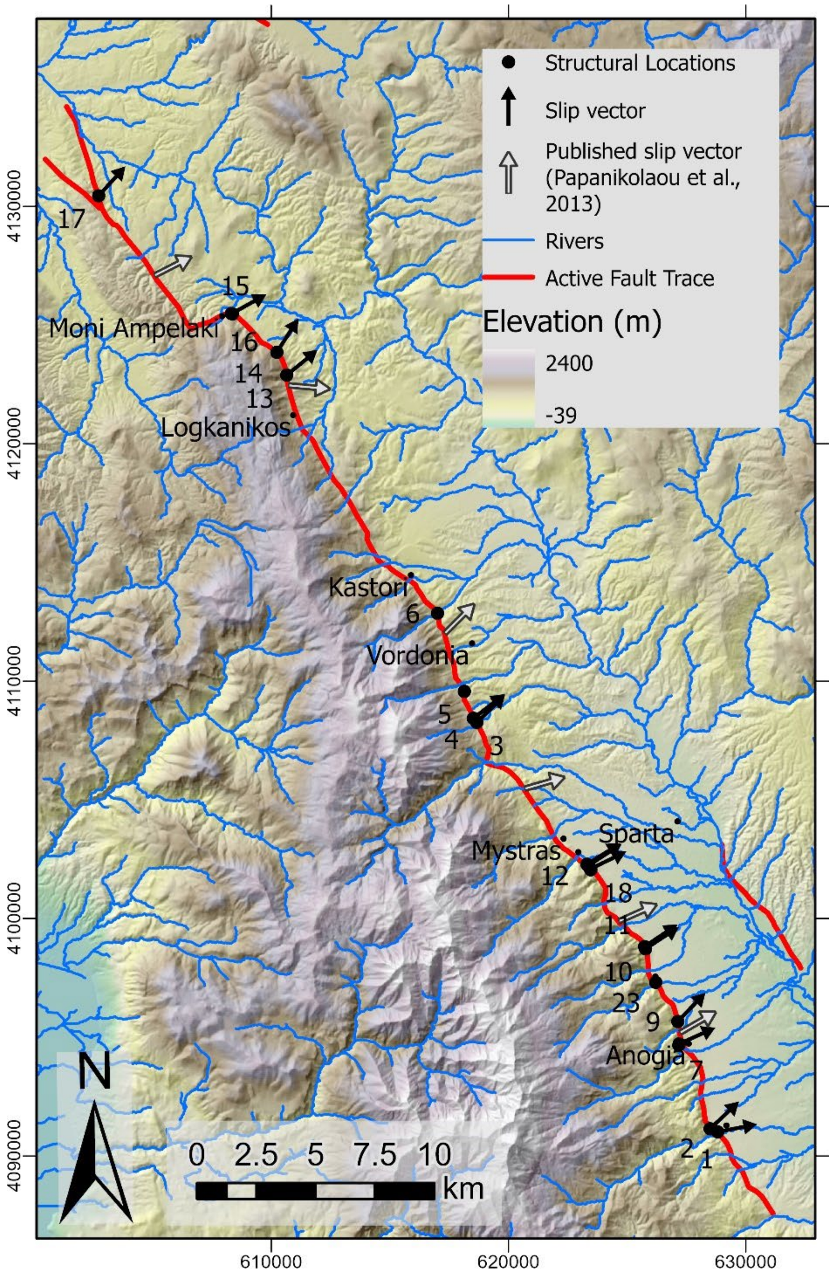

Figure 3. The Sparta Fault and locations where fault measurements were taken. The DEM is the 30 m ALOS World3D30 ©JAXA projected in UTM zone 34 N. Slip vectors as reported by Papanikolaou et al. (2013) are also included. For overall location map see figure 1A.

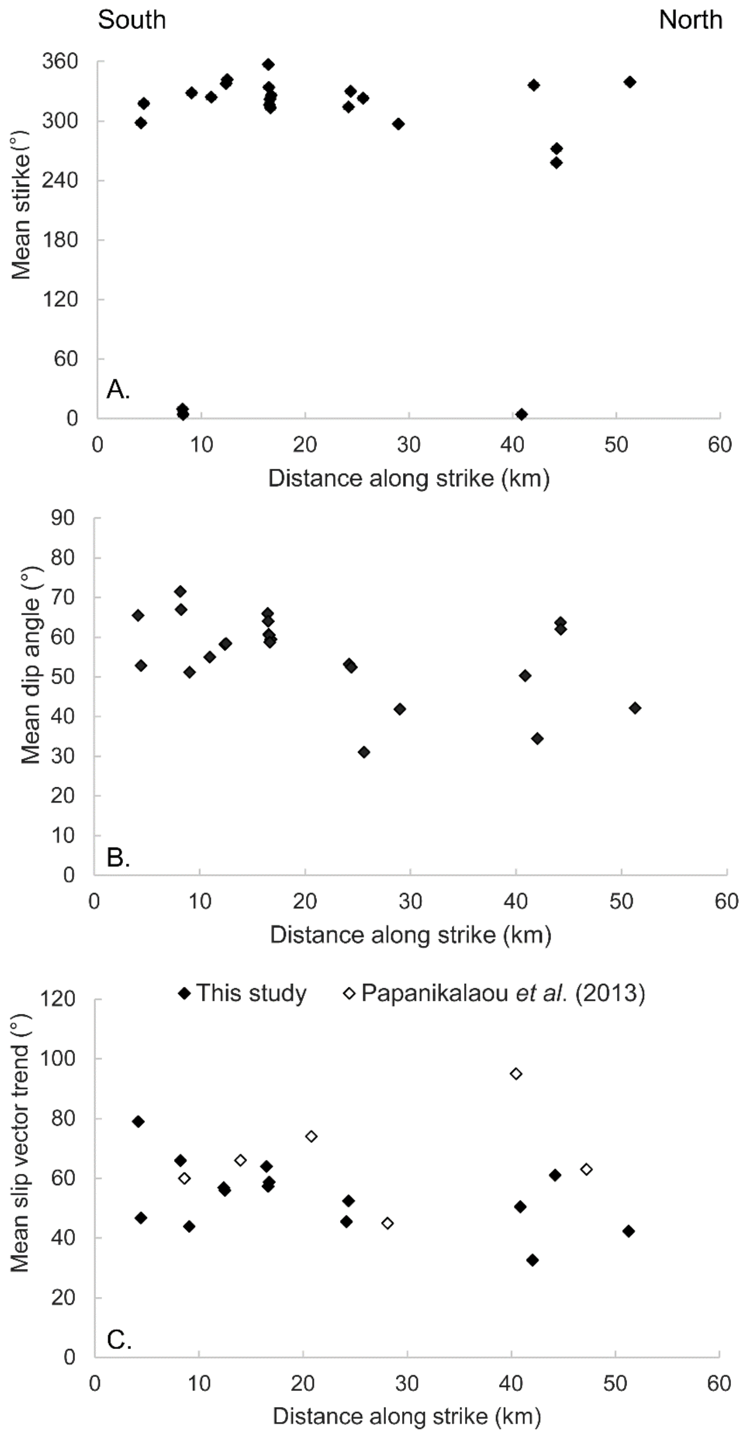

Figure 4: Mean values of A) strike and B) dip angle along the Sparta Fault from south to north and C) mean values of the measured slip vector.

Figure 5. Photographs of the fault. A) View from the southern tip of the fault looking north showing the clear escarpment and location of the active fault (black arrow), B) View of the post-glacial fault scarp exposed at the base of the escarpment north of Anogia (location 9); C) View to the west showing the post-glacial fault scarp exposed on a steep hillside south of Parori. D) View of the fault south of Vordonia, where the angle of dip is 30 - 40° (location 5). E) Oblique view of the fault scarp at Moni Ampleki that has a throw of 7.53 m (location 16). F) Road exposure of the fault plane near Moni Ampleki, note natural exposure towards the top of the plane (location 15).

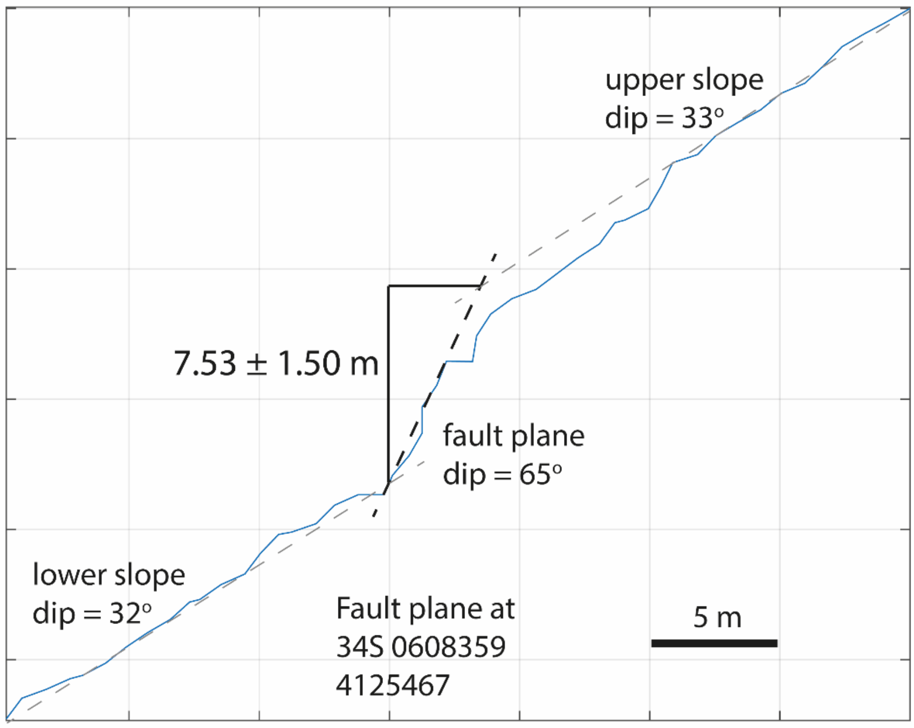

Figure 6: Topographic profile taken across the post-glacial fault scarp at 0608359 4125467 (location 16) in the northern section of the Sparta fault. The post-glacial throw is interpreted to be 7.53 ± 1.50 m.

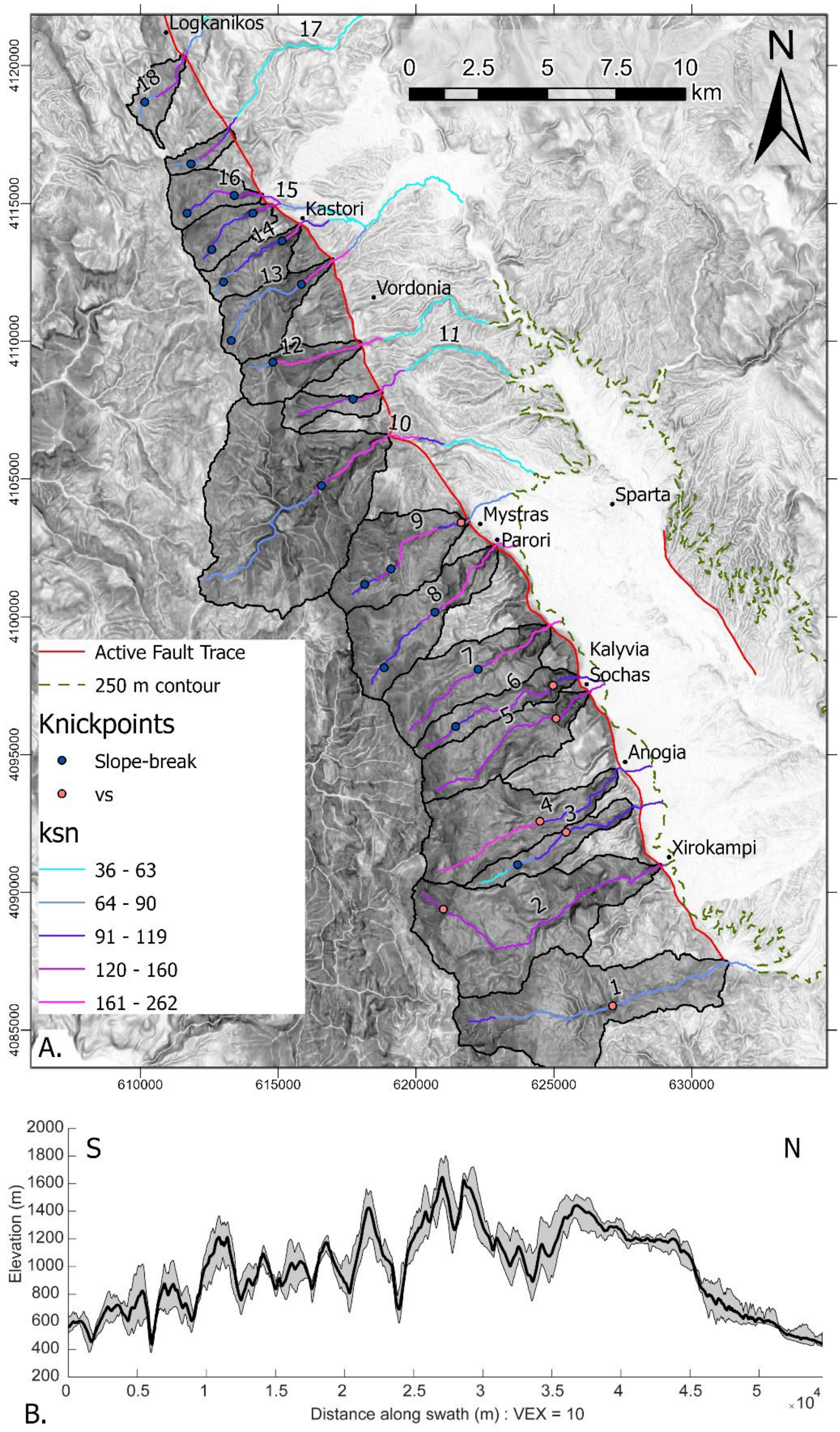

Figure 7A. Greyscale slope map of the Sparta region derived from the 30 m ALOS World 3D30 DEM ©JAXA, showing the rivers and knickpoints extracted for analysis and the 250 m contour used as the base-level for the rivers. B. Topographic swath profile showing the variation in elevation along the strike of the fault from south to north.

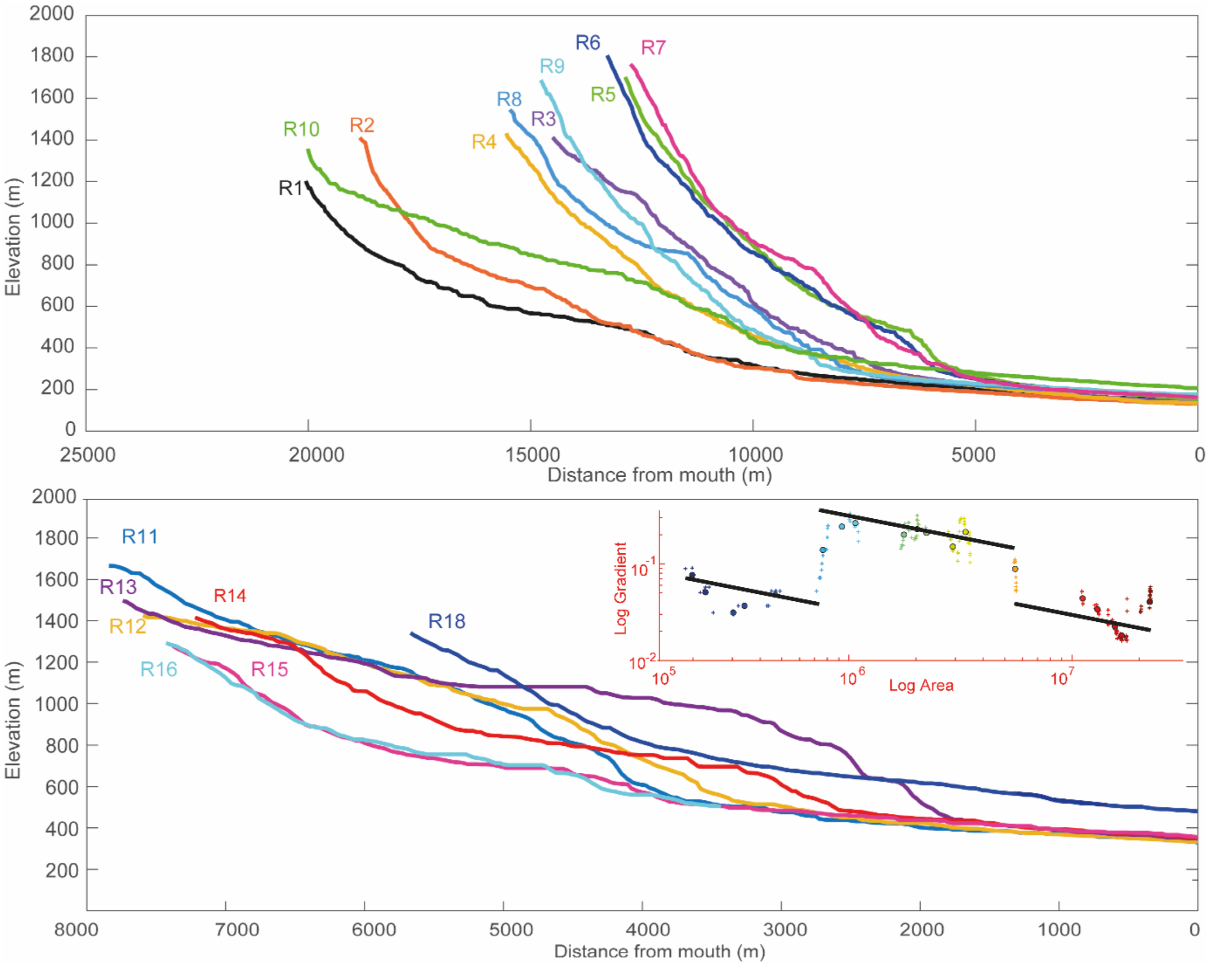

1872

1873 Figure 8 – River long profile(s) of the 18 rivers extracted including an inset of slope-area graph

1874 illustrating a knickpoint with a slope-break morphology (river 18).

Figure 9: A) a general view of river 10 looking upstream within the knickzone; note the lack of bedload in the steep bedrock channel, B) river 10 upstream of the slope-break knickpoint, note the significant bedload composed of cobbles, pebbles and finer grains. C) river 10 close to the fault zone showing the base of the vertical-step knickpoint (i.e., the waterfall).

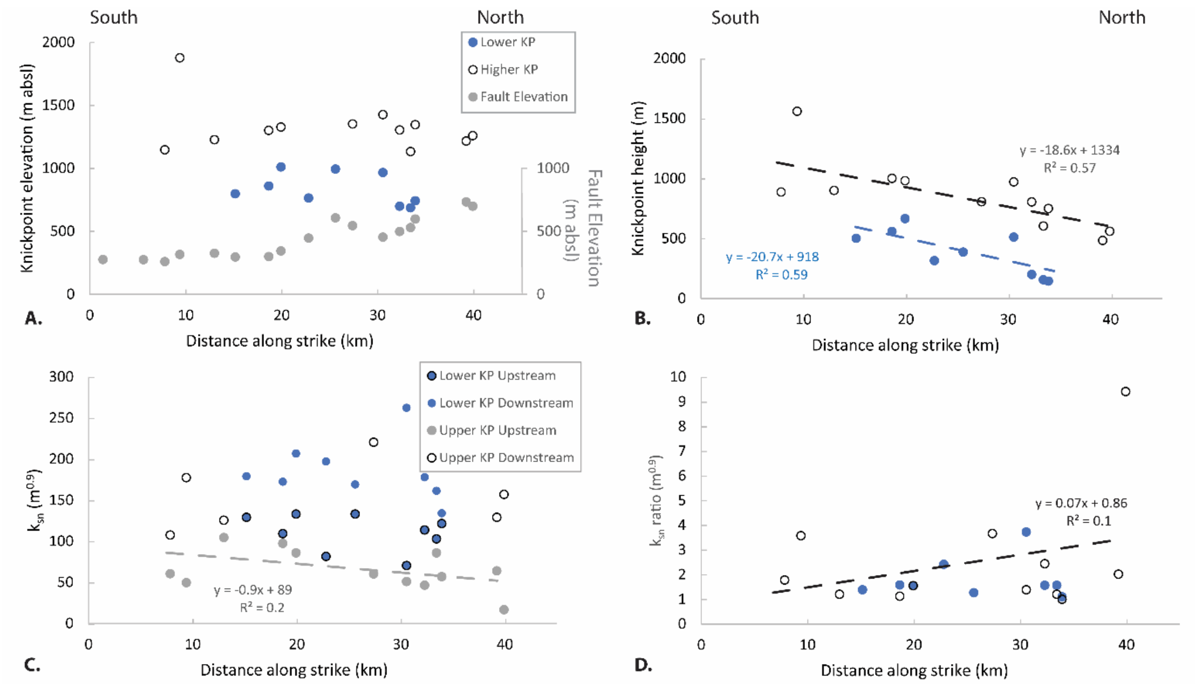

Figure 10. Comparison of various geomorphic variables along the strike of the Sparta Fault from south to north for the two knickpoint populations - the lower and higher knickpoints; a) knickpoint and fault elevation above sea level, b) knickpoint height (the difference between the fault and knickpoint elevations), c) normalised steepness index (k_{sn}) above and below the knickpoint and d) the ratio of k_{sn} across the knickpoint.

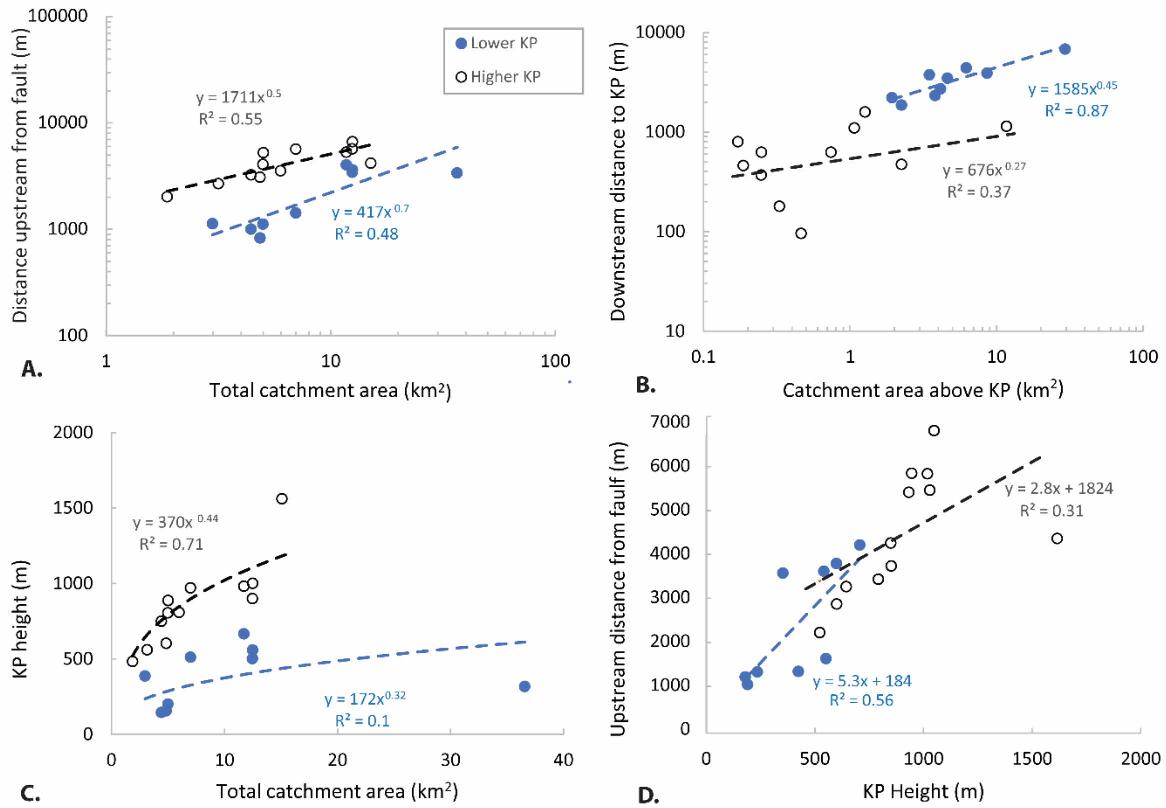

Figure 11: Graphs showing a number of knickpoints variables for the rivers crossing the Sparta fault, where the higher knickpoint is shown with the open symbol and the lower in the closed symbol; A) distance from the fault against the total catchment area, B) downstream distance from the divide against catchment area above the knickpoint, C) knickpoint height against the total catchment area, D) distance upstream from the fault against knickpoint height.

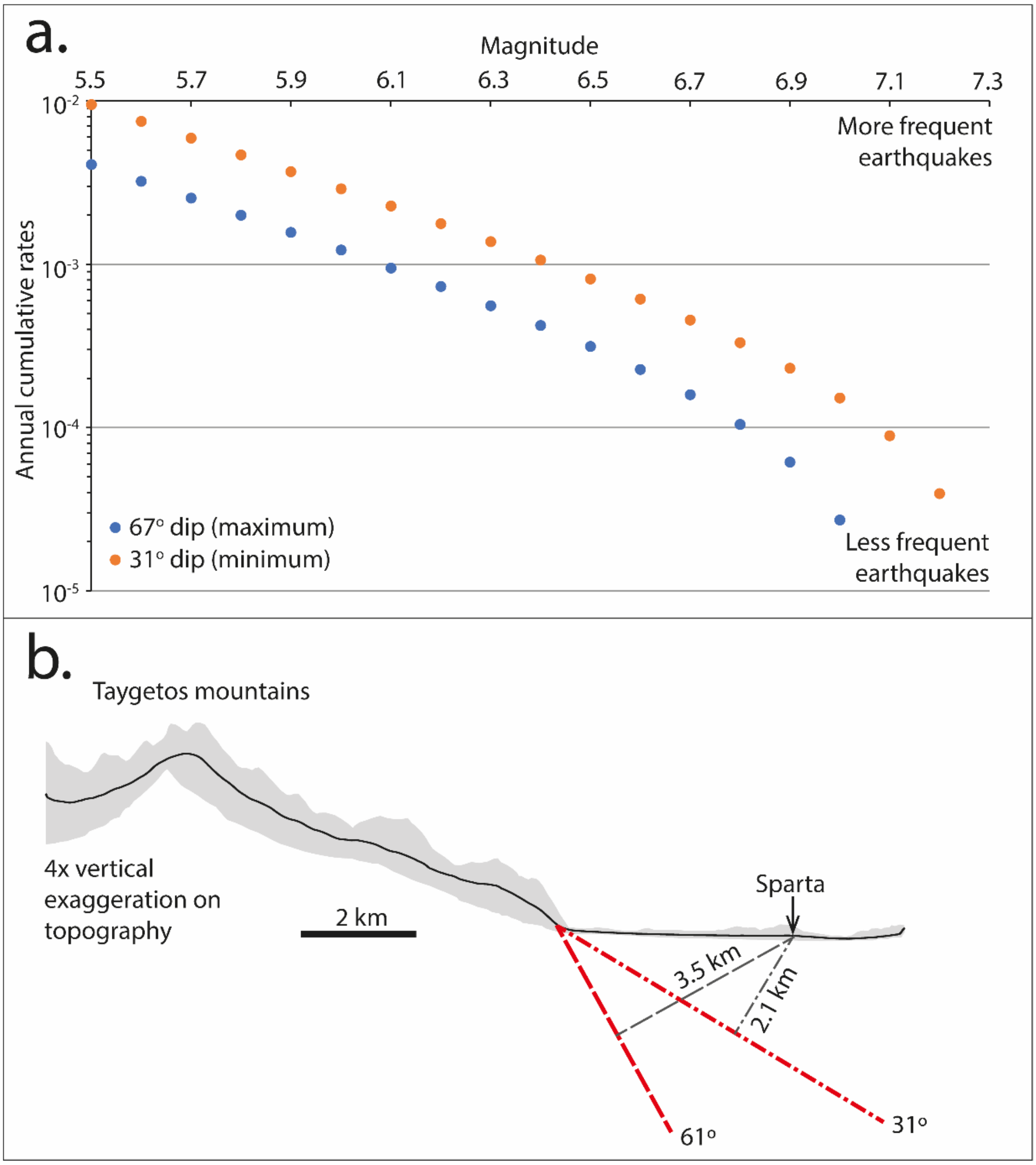

Figure 12. Seismic hazard calculations for the Sparta fault. A). annual cumulative rates of earthquake occurrence for earthquakes M>5.5 for a steeply and shallowly dipping fault. The shallower the fault dip, the more frequently earthquakes are expected to occur. b). uncertainty in dip manifests as uncertainty in the source-to-site distance between the Sparta fault and Sparta city.

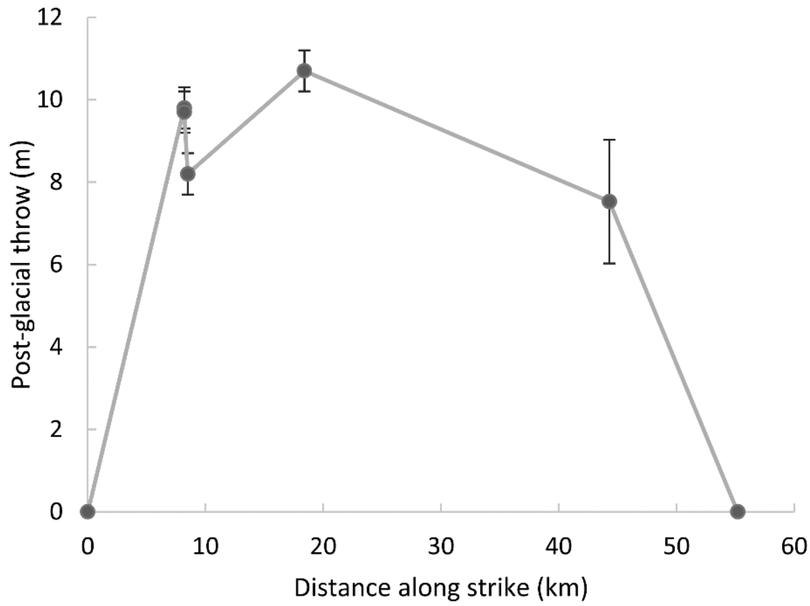

Figure 13. Post-glacial throw as determined along the strike of the Sparta Fault from this and the previous studies of Benedetti et al. (2002) and Papanikalaou et al. (2013), with a line shown to interpret the overall throw profile of the fault. Note: the curve is pinned to the inferred tip locations where throw is assumed to be zero.